

A Coupled Atmosphere–Ocean GCM Study of the ENSO Cycle

JIN-YI YU AND CARLOS R. MECHOSO

*Department of Atmospheric Sciences, University of California, Los Angeles,
Los Angeles, California*

(Manuscript received 13 March 2000, in final form 25 September 2000)

ABSTRACT

This study examines interannual variability produced by a recent version of the University of California, Los Angeles, coupled atmosphere–ocean general circulation model (CGCM). The CGCM is shown to produce ENSO-like climate variability with reasonable frequency and amplitude. A multichannel singular spectrum analysis identifies the simulated ENSO cycle and permits examination of the associated evolution of atmospheric and oceanic states. During the cycle, the evolution of upper-ocean heat content in the tropical Pacific is characterized by a zonal oscillation between the western and eastern equatorial Pacific and a meridional oscillation between the equator and 10°N. The zonal oscillation is related to the amplification of the cycle, and the meridional oscillation is related to the transition between phases of the cycle. It is found that the north–south ocean heat content difference always reaches a threshold near the onset of a warm/cold event.

The three-dimensional evolution of ocean temperature anomalies in the tropical Pacific during the simulated ENSO cycle is characterized by four major features: 1) a build up in the subsurface of the western equatorial sector during the pre-onset stage, 2) a fast spread from the western subsurface to the eastern surface along the equator during the onset stage, 3) a zonal extension and amplification at the surface during the growth stage, and 4) a northward and downward spread during the decay stage.

Ocean temperature budget analyses show that the buildup of subsurface temperature anomalies is dominated by the vertical advection process in the western sector and the meridional advection process in the central sector. The former process is associated with vertical displacements of the thermocline, which is an important element of the delayed oscillator theory. The latter process is associated with a Sverdrup imbalance between trade wind and thermocline anomalies and is emphasized as the primary charge–discharge process by the recharge oscillator theory. It is argued that both processes play key roles in producing subsurface ocean memory for the phase transitions of the ENSO cycle.

1. Introduction

The El Niño–Southern Oscillation (ENSO) phenomenon has long been recognized as the major interannual climate variation of the coupled ocean–atmosphere system [Bjerknes (1969); Wyrtki (1975); see Philander (1990) for a review]. Warm (El Niño) and cold (La Niña) ENSO events occur quasi-periodically and are generally associated with significant anomalies in global weather patterns. Recognition of the importance of ENSO accelerated work toward successful simulations of the climate system with coupled atmosphere–ocean general circulation models (CGCMs). The work targeted both the seasonal cycle and interannual variability of the system in the understanding that these are not independent aspects of the issue. Progress has been rapid, and the problem of climate drift in many models has been great-

ly alleviated [compare results presented in Neelin et al. (1992) and Mechoso et al. (1995)]. In addition, several contemporary CGCMs are capable of producing ENSO-like variability without artificial flux corrections at the atmosphere–ocean interface (e.g., Philander et al. 1992; Latif et al. 1993; Yu and Mechoso 1998). Those successes strongly suggest that key components of the ENSO phenomenon are captured by contemporary CGCMs and that the models have matured to the extent that their products can be used for a critical examination of theories on ENSO.

The current paper presents the simulation of ENSO by a recent version of the University of California, Los Angeles, (UCLA) CGCM, whose atmospheric model component was extensively revised in recent years (see Yu et al. 1997; Fararra et al. 1997; Li et al. 1999; Mechoso et al. 2000). The first part of the paper describes the model, simulation performed and the interannual climate variability produced. The atmospheric and oceanic structures that compose the simulated ENSO cycle are extracted from the model results. As in observations, the simulated cycle comprises complex correlated atmospheric and oceanic structures. An effective statis-

Corresponding author address: Dr. Jin-Yi Yu, Dept. of Atmospheric Sciences, 7127 Math Sciences Building, 405 Hilgard Ave., Los Angeles, CA 90095-1565.
E-mail: yu@atmos.ucla.edu

tical method, therefore, is needed to extract the quasi-periodic phenomenon from simulated fields. For this work, we have selected the multichannel singular spectrum analysis method (M-SSA; Broomhead and King 1986; Vautard and Ghil 1989), which has been shown capable of extracting near-periodicities, and their associated spatio-temporal structures, from short and noisy time series (Robertson et al. 1995a). The M-SSA method is an extension of the principal component analysis of a time series of spatial vectors to include additionally an analysis of temporal structure (Keppenne and Ghil 1992).

The second part of the paper focuses on the simulated ENSO dynamics by analyzing the relationships between evolutions of atmospheric and oceanic structures. A considerable number of theoretical and modeling studies have already been performed in an intense effort to understand the dynamics of ENSO. Those theories have emphasized the growth and phase-transition mechanisms at work during the cycle. The former mechanism is responsible for the amplification of anomalies during the warm or cold phases of the cycle, while the latter is responsible for the vacillation between phases. Amplitudes and recurring timescales of ENSO events are determined by the combined effects of these two mechanisms. It is generally agreed that coupled instabilities of the atmosphere–ocean system provide the growth mechanism, as first postulated by Bjerknes (1969). Accordingly, small perturbations in sea surface temperature (SST) over the equatorial Pacific amplify through positive feedbacks with associated perturbations in surface winds and convection.

The phase-transition mechanism is less understood at present. At least three candidate mechanisms have been suggested from conceptual or highly simplified studies [see Neelin et al. (1998) for a review on ENSO theories]. Although most ENSO theories agree that the ocean provides the memory for the low-frequency oscillation of the cycle, they assign the role of carrying that memory to different processes. The delayed oscillator theory (Schopf and Suarez 1988; Battisti and Hirst 1989) suggests that the delayed negative feedback associated with free oceanic equatorial wave propagation and reflection at the western boundary is responsible for the phase reversal of the ENSO cycle. The slow SST–fast wave theory (Neelin 1991; Neelin and Jin 1993; Jin and Neelin 1993a,b) argues that oceanic surface thermodynamics, rather than ocean wave dynamics, provide the memory for the phase transition. There also has been a recent revival of interest in the recharge oscillator theory (Wyrtki 1975; Zebiak and Cane 1987; Zebiak 1989; Jin 1997). This theory is conceptually similar to the delayed oscillator theory in suggesting the importance of subsurface ocean adjustment processes in producing the needed delay for ENSO oscillation. The recharge oscillator, on the other hand, emphasizes the importance of the buildup (i.e., charge) and release (i.e., discharge) of zonal-mean ocean heat content in the equatorial band

for the phase reversal of the ENSO cycle. Moreover, the charge and discharge are generated by the nonequilibrium between the zonal-mean ocean heat content and trade wind system. A critical analysis of the phase-transition mechanisms suggested by the different theories requires comprehensive and basinwide information of both surface and subsurface ocean states, to an extent that is currently unavailable from observations. The complete atmospheric and oceanic information produced by CGCM simulations is a most useful alternative (e.g., Collins 2000). For this purpose, we use the simulated results to examine the correlations among SST, atmospheric heat flux, and wind stress forcings, and upper-ocean heat content during the ENSO cycle.

We start in section 2 by describing the CGCM and the simulation. Section 3 examines the seasonal cycle and interannual variability produced in the simulation. Section 4 discusses the spatial and temporal structures of the leading oscillatory mode detected by the M-SSA method in the simulated fields. The relationships between atmospheric and oceanic anomalies during different phases of the cycle are discussed in section 5. The three-dimensional evolution of simulated ocean temperature in the tropical Pacific is shown in section 6. An ocean temperature budget analysis is performed in section 7 to identify the primary contributors to ocean temperature variations during the ENSO cycle. Section 8 gives a summary and discussion of the results.

2. Model and simulation

The CGCM used in this study consists of the UCLA global atmospheric GCM (AGCM; Suarez et al. 1983; Mechoso et al. 2000, and references therein) and the oceanic GCM (OGCM) known as GFDL Modular Ocean Model (MOM) (Bryan 1969; Cox 1984; Pacanowski et al. 1991). The AGCM includes the schemes of Deardorff (1972) for the calculation of surface wind stress and surface fluxes of sensible and latent heat, Katayama (1972) for shortwave radiation, Harshvardhan et al. (1987) for longwave radiation, Arakawa and Schubert (1974) for parameterization of cumulus convection, and Kim and Arakawa (1995) for parameterization of gravity wave drag. The model has 15 layers in the vertical (with the top at 1 mb) and a horizontal spacing of 4° lat \times 5° long. The MOM includes the scheme of Mellor and Yamada (1982) for parameterization of sub-grid-scale vertical mixing by turbulence processes. The surface wind stress and heat flux are calculated hourly by the AGCM, and the daily averages passed to the OGCM. The SST is calculated hourly by the OGCM, and its value at the time of coupling is passed to the AGCM. The ocean model domain covers the tropical Pacific from 30° S to 50° N, and from 130° E to 70° W. The model has 27 layers in the vertical with 10-m resolution in the upper 100 m. The ocean has constant depth of about 4150 m. The longitudinal spacing is 1° , the latitudinal spacing varies gradually from $\frac{1}{3}^\circ$ between

10°S and 10°N to almost 3° at 50°N. The time-varying climatology from Alexander and Mobley (1976) is used to prescribe the SSTs outside the OGCM domain. No “ad-hoc corrections” are applied to the information exchanged by model components.

The AGCM used in this study includes several recent and important revisions in the physical parameterizations. The model version used in earlier CGCM studies (e.g., Robertson et al. 1995a,b; Ma et al. 1996; Yu and Mechoso 1999a,b) significantly underestimated subtropical marine stratocumulus in the planetary boundary layer (PBL; see Ma et al. 1996; Yu and Mechoso 1999b for discussions). The revised formulation of PBL and stratocumulus processes of Li et al. (1999) has alleviated this problem. AGCM simulations performed with this revised PBL formulation have shown better agreement with observations in the geographic distribution and frequency of stratocumulus clouds. Also, the AGCM versions used in earlier CGCM studies significantly underestimated the ozone concentration predicted in the upper troposphere and lower stratosphere. The shortwave absorptivity of ozone was also too large. To reduce these two problems, Farrara et al. (1997) prescribed ozone from a zonally averaged climatology, replaced the formulation of Katayama (1972) for shortwave absorptivity of ozone by that of Lacis and Hansen (1974), and introduced the parameterization of Manabe and Möller (1961) for calculation of the shortwave absorption by water vapor. In addition, they added momentum to the list of variables that are vertically mixed in dry, convectively unstable layers. Those revisions in radiation and ozone processes have a larger impact on the simulation of the stratospheric circulation but also improve results in the troposphere.

A new version of the UCLA CGCM was produced using the revised AGCM, and a 53-yr long integration was performed with this model. The initial oceanic condition is an ocean at rest with climatological January distributions of temperature and salinity corresponding to the climatology compiled by Levitus (1982). The initial atmospheric condition is obtained by integrating the AGCM from an analysis of 15 October 1979 to 15 January of the following year. To reduce the influences from model spinup, only SSTs from year 13 to year 52 are used for analysis in this paper. All OGCM outputs are interpolated horizontally to the AGCM grids in order to facilitate the analyses of air–sea interactions and to reduce the size of matrices in the M-SSA analysis.

3. Simulated seasonal cycle and interannual variability

Figure 1 presents the long-term mean simulated SSTs for April and October. The patterns and magnitudes of SSTs in both panels of Fig. 1 compare well with the observed except in the eastern Pacific south of the equator, where simulated values are too high. The October field includes a well-developed cold tongue in the east-

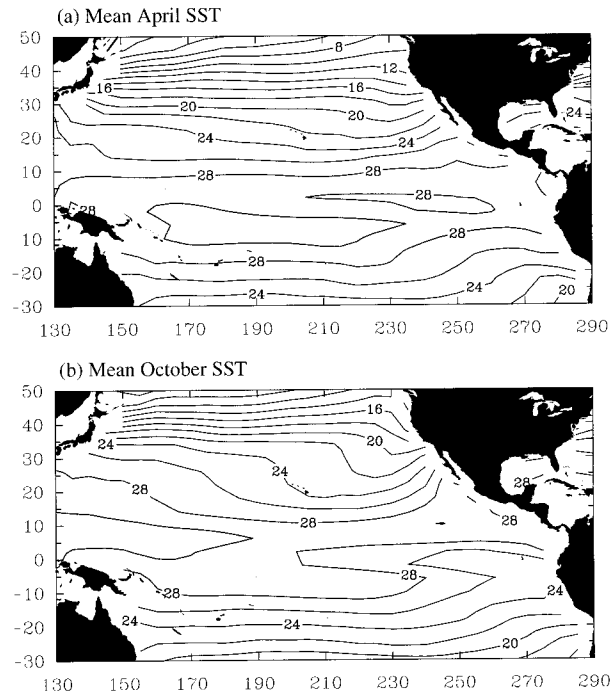


FIG. 1. Long-term monthly means of simulated SST for (a) Apr and (b) Oct. Contour interval is 2 K. Values greater than 28°C are shaded.

ern equatorial Pacific. Overall, these results are more realistic than those obtained with earlier versions of the UCLA CGCM (cf. Robertson 1995a; Mechoso et al. 1995), which were characterized by a significant cold bias in SST in association with excessive surface evaporation (Yu and Mechoso 1999a). The revisions in the PBL parameterization result in moister PBL air and decreased evaporation from the ocean surface.

The warm bias in the eastern Pacific south of the equator remains significant, although it is much reduced in comparison with that in previous model versions. The sensitivity studies of Ma et al. (1996) and Yu and Mechoso (1999b) linked this warm bias to the underestimation of Peruvian stratocumulus. The PBL revisions have resulted in improved simulation of those subtropical clouds (see Li et al. 1999) in uncoupled AGCM simulations. The improvement obtained in the CGCM, however, is not as dramatic as that in the AGCM with prescribed SSTs. Such a difference in model behaviors is at least partially due to the strong positive feedbacks between marine stratocumulus and the underlying SSTs (Philander et al. 1996). In the CGCM, clouds whose radiative properties are not captured properly will result in erroneous SSTs, which, in turn, will affect subsequent cloud formation. In the uncoupled AGCM simulations, on the other hand, clouds do not affect the SSTs. The improvement after the PBL revisions extends to the annual variations of SST in the equatorial eastern Pacific. For example, the asymmetric features between the warm and cold phases of the equatorial cold tongue discussed

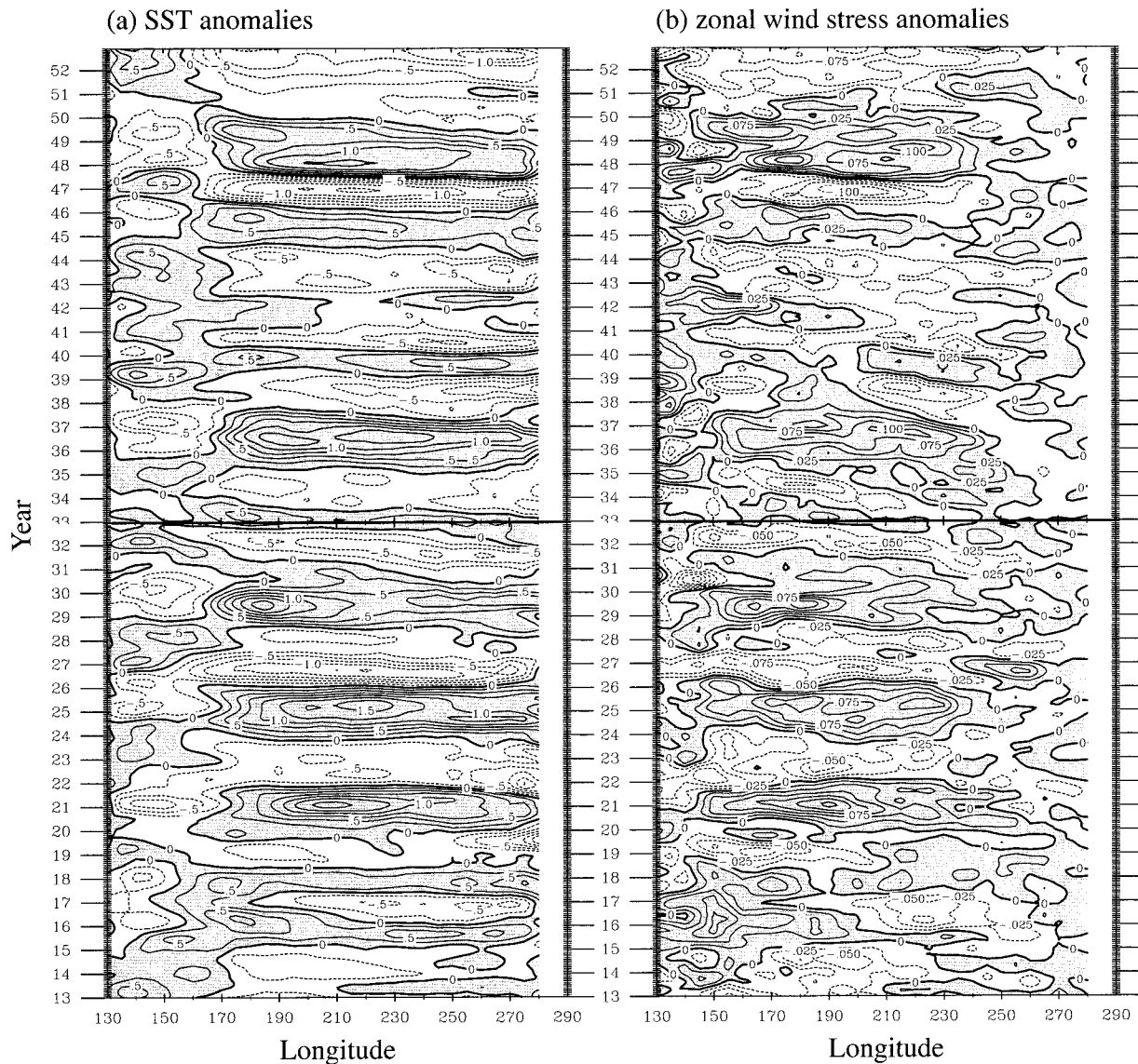


FIG. 2. Longitude–time cross sections of simulated (a) SST anomalies and (b) zonal wind stress anomalies. Anomalies from years 13 to 52 are shown. Annual cycles are removed. A low-pass filter is applied to remove anomalies with timescales shorter than one year. Contour intervals are 0.25°C for SST and $0.025 \text{ dyn cm}^{-2}$ for zonal wind stress. Positive values are shaded.

by Yu and Mechoso (1999b) are better captured (not shown). The westward propagation speed of SST deviations from the annual mean is stronger in the warm phase than in the cold phase, and the maximum SST deviations in the cold phase last longer.

Figure 2 shows the time evolution of simulated SST and zonal wind stress anomalies in the equatorial band between 4°S and 4°N . Here, anomalies are defined as the departures from the the mean annual cycle. A low-pass filter was applied to the anomalies to remove the variability with timescales shorter than one year. Figure 2a shows stronger SST anomalies in the eastern-to-central sector, with peak strength around 150°W . The largest amplitude of SST anomalies is close to 2°C , which is almost four times as large as the strongest anomalies

produced by earlier model versions (Robertson et al. 1995b). This improvement is consistent with the notion that an accurate simulation of the mean state and annual cycle of the coupled atmosphere–ocean system is crucial for better ENSO simulations (e.g., Meehl 1990; Jin et al. 1994; Tziperman et al. 1994). Anomalous warm SST events develop approximately every 3–4 yr (at yr 21, 25, 29, 33, 36, 40, 45, 48). This recurrence frequency of the simulated warm events is close to that of observed El Niño events (Rasmusson and Carpenter 1982).

According to Fig. 2b, most wind stress anomalies are confined to the western part of the ocean basin, with largest amplitudes close to 0.2 dyn cm^{-2} . It is apparent that all major warm events are accompanied by strong westerly wind stress anomalies to the west of the max-

imum SST anomalies. The ratio between largest magnitudes of wind and SST anomalies is about $0.1 \text{ dyn cm}^{-2} (\text{°C})^{-1}$ which is comparable to that obtained by earlier versions of the CGCM that produced *both* weaker wind stress and SST anomalies (Robertson et al. 1995b). Therefore, if this ratio is interpreted as a measure of the strength of atmosphere–ocean coupling, the increase of interannual variability in the present CGCM is not primarily due to stronger feedbacks between SST and wind stress anomalies.

Figure 3 shows the evolution of SST anomalies during the warm event that develops during year 24 of the simulation, which is among the strongest produced by the CGCM. The warming starts along the South American coast and central Pacific in the earlier part of the year (Fig. 3a), and it extends toward the central equatorial Pacific during the following few months (Fig. 3b). A local maximum in SST anomalies appears in the eastern equatorial Pacific in October. After this month, SST anomalies start to decrease in the eastern sector but continue to increase in the central sector to a maximum of 1.5°C in the following February (Fig. 3c). (The SST anomalies before the low-pass filtering is close to 2°C .) The event begins to decay in the spring and is over before the end of the year (Figs. 3d,e). The spatial structure and time evolution of the model simulated warm event are reasonably similar to those observed during El Niño. The model, however, produces a weaker eastward propagation of the warm anomalies and tends to place the strongest SST anomalies in the central equatorial Pacific. In addition, the interevent variability is weaker than observed. Most simulated events tend to start in the northern spring and the associated anomalies tend to grow to their maximum strength in the following autumn season. The simulated warm events, therefore, exhibit a phase locking with the seasonal cycle that is close to that of observed El Niño events (Rasmusson and Carpenter 1982).

4. The simulated ENSO cycle

To extract the multivariate structure associated with the simulated ENSO cycle we apply the M-SSA method to combined atmospheric and oceanic variables between 20°S and 20°N . In this way, the correlative relationships between the atmosphere and ocean during the cycle can be examined. The atmospheric variables included in the input to M-SSA are the zonal and meridional components of surface wind stress and net surface heat flux. They represent the dynamical and thermal forcings (as well as response) of the atmosphere to the ocean. The oceanic variables include SST and ocean heat content, which is defined as the vertically averaged temperature in the upper 300 m. The 20°S – 20°N band is selected in order to explore the possibility that the underlying ENSO dynamics involves both the equatorial and off-equatorial Pacific. The anomalies are low-pass filtered before the M-SSA method is applied. In addition, all

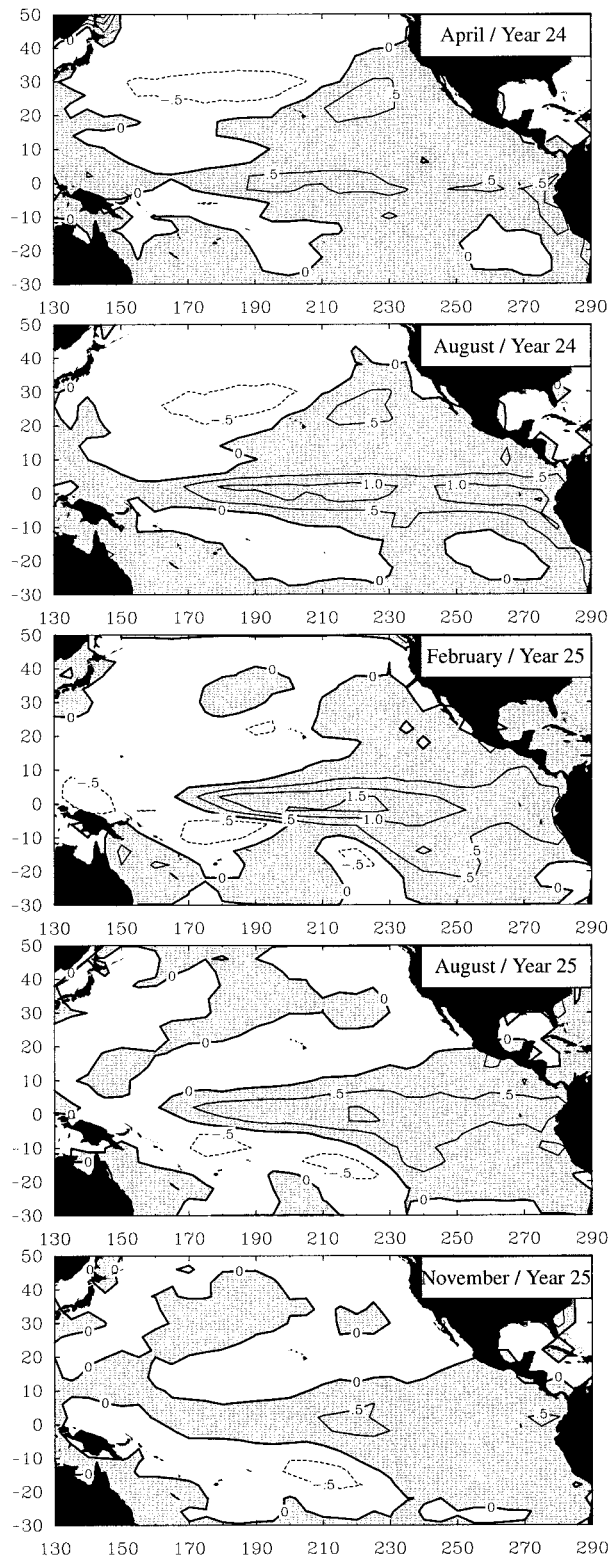


FIG. 3. Evolution of SST anomalies during the warm event in year 24 of the simulation. SST anomalies are obtained by removing the annual cycle and by filtering out variations with timescales shorter than 1 yr^{-1} . Contour intervals are 0.5°C . Positive values are shaded.

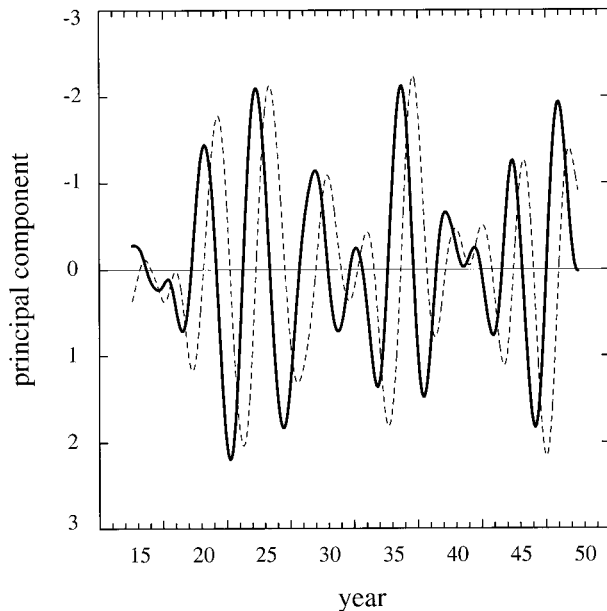


FIG. 4. Principal components of the first (solid) and the second (dashed) eigenvector obtained from the combined 5-variable M-SSA analysis.

fields are scaled by appropriate constants to ensure that their values have similar magnitudes. The scaling factors are 1, 1, 0.05, 10, and 10 for SST, ocean heat content, surface heat flux, and zonal and meridional wind stress, respectively. The scaling factors are then taken out from the M-SSA modes. We use a 61-month window in the M-SSA, as suggested by Robertson et al. (1995a) to analyze interannual variability.

An oscillatory mode is characterized in M-SSA by a pair of eigenvectors with similar eigenvalues and principal components (PCs). The first two leading eigenvectors of the combined five-variable M-SSA explain approximately the same amount of variance (i.e., eigenvalues), and their PCs are also very similar to each other, except for a phase shift (Fig. 4). Therefore, the first pair of the eigenvectors represents an oscillatory mode that explains 23% of the variance in the combined variables. A power spectrum analysis of the PCs (not shown) reveals a dominant period of about 48 months. This is very close to the reoccurrence timescale of the ENSO-like SST anomalies in the simulation (see Fig. 2a).

Figure 5 shows the structure of this oscillatory mode along the equator during the 61-month window lag used in the M-SSA. The modal structure of SST is characterized by weakly westward-propagating anomalies in the central-to-eastern sector and by quasi-standing anomalies with opposite signs along the western end of the basin (Fig. 5a). SST anomalies in the western sector lag those in the center and east sectors by about 6 months. Large westerly (easterly) wind stress anomalies appear almost simultaneously to the west of positive (negative) SST anomalies in the central-to-eastern sector

(Fig. 5b). The patterns of SST and zonal wind stress eigenvectors are similar to those of the anomaly fields shown in Fig. 2. Therefore, the leading oscillation mode obtained by the M-SSA represents the ENSO cycle produced by the CGCM and can be identified with the observed phenomenon.

Figures 5a and 5c show that strongest positive (negative) SST anomalies in the central sector are flanked by centers of southward (northward) meridional wind stress anomalies. The strongest center in the west coincides with the strongest zonal wind stress anomalies (Fig. 5b). The values shown in Fig. 5c are representative of the meridional wind stress at 2°S . Meridional wind stress anomalies at 2°N and 2°S have opposite signs (not shown), and the former have smaller magnitude than the latter. Figure 5d shows that surface heat flux anomalies (positive downward) are out of phase with SST anomalies, hence providing a negative feedback during the cycle. The coincidence between centers of largest heat flux and wind stress anomalies suggests that the primary contribution to the negative SST-heat flux feedback comes from anomalous evaporation.

Figure 6 shows the combined SST and wind stresses fields in the entire tropical Pacific during various stages of the warm and cold phases of the oscillation mode. In the onset stage of the warm phase, positive SST anomalies develop in the eastern equatorial sector (Fig. 6a). The anomalies expand rapidly toward the date line during the growing stage with the largest values still along the South American coast (Fig. 6b). In the mature stage, the center of largest SST anomalies moves toward the date line and negative anomalies appear in the western equatorial Pacific and around the pool of warm anomalies (Fig. 6c). In the decaying stage, positive SST anomalies detach from the South American coast first and then weaken in the central sector (Fig. 6d). Zonal wind stress anomalies tend to point toward the center of largest SST anomalies, while meridional wind stress anomalies point toward the equator from both the northern and southern Tropics. Also, large wind stress anomalies in both the equatorial and off-equatorial Pacific are confined to the west of the eastern edge of the SST anomaly center. The onset and mature stages of the cold phase are approximately the mirror image of those for the warm phase, with wind stress vectors pointing away from the equator.

5. Evolution of ocean heat content anomalies

A better understanding of the evolution of ocean heat content anomalies and its relationship with that of SST anomalies during the simulated ENSO can provide insight into the processes that carry the memory of the cycle. Figure 7a shows the eigenvector structure of the former anomalies at the equator obtained from the leading oscillatory M-SSA mode. Positive and negative values propagate slowly eastward and their arrival at the eastern boundary is almost simultaneous with the onset

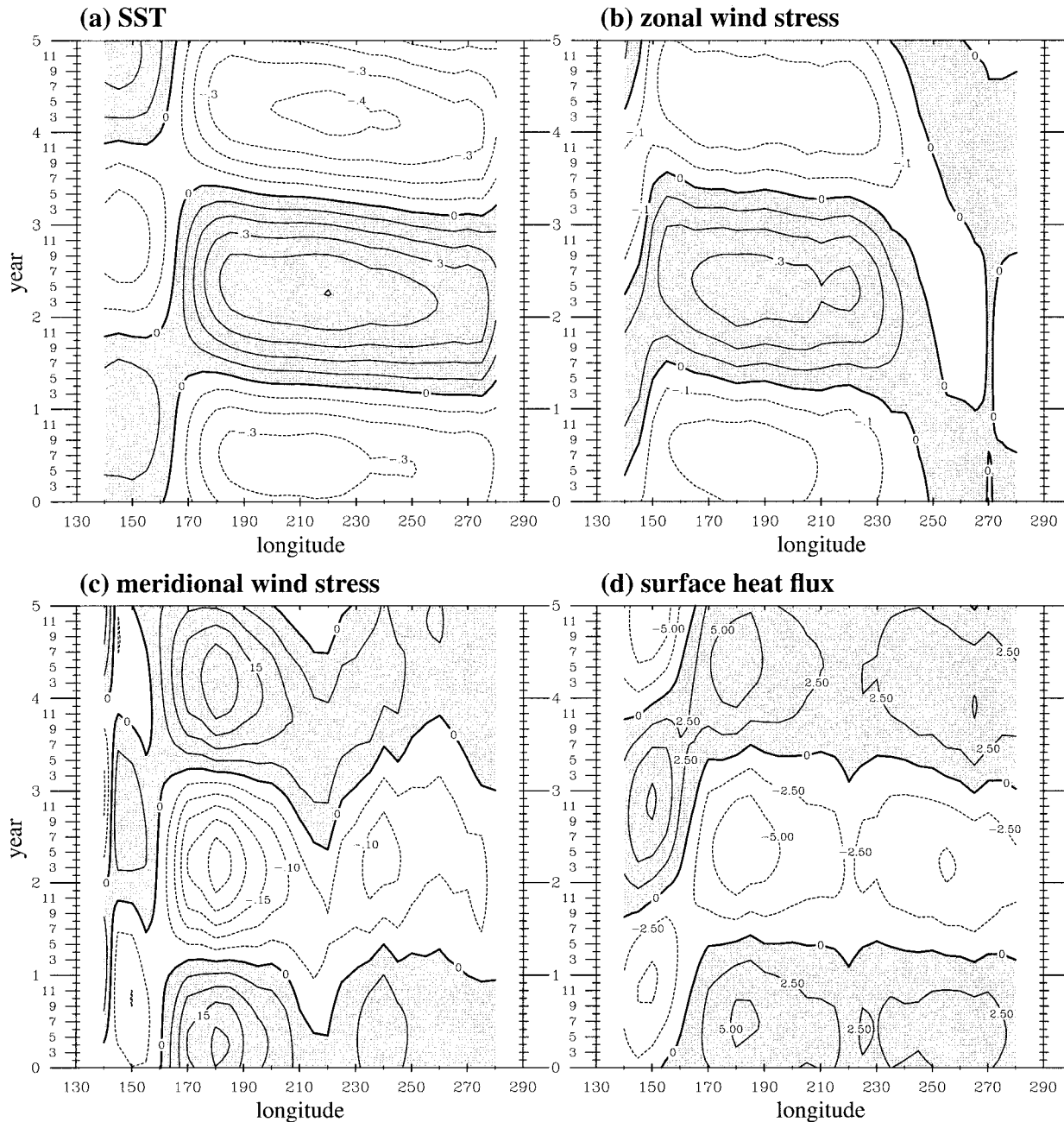


FIG. 5. The eigenvectors of the leading oscillation mode along the equatorial Pacific obtained from the combined 5-variable M-SSA: (a) SST, (b) zonal wind stress, (c) meridional wind stress, and (d) surface heat flux. The vertical coordinate spans the 61-month window lag used in M-SSA. Contour intervals are 0.10°C for (a), 0.01 dyn cm^{-2} for (b), $0.005 \text{ dyn cm}^{-2}$ for (c), and 2.5 W m^{-2} for (d). Values shown in (b) and (c) are scaled by 10. Positive values are shaded.

of the warm and cold phases of the ENSO cycle, respectively (see Fig. 5a). The evolution shown in Fig. 7a is in qualitative agreement with the behavior predicted by the delayed oscillator [see Fig. 7 of Battisti and Hirst (1989)].

The two centers of large anomalies in the western and eastern sectors, however, appear to develop more in situ than via propagation. A further separation into zonal-

mean and zonally asymmetric components shows that the eastward propagation depicted in Fig. 7a can be interpreted as the superposition of oscillations in the zonal-mean component and in the east–west contrast of the anomalies. Figure 7b reveals that the zonal-mean component increases gradually before the onset of the warm phase of the cycle to a maximum that is reached about the time when onset occurs. As the warm phase

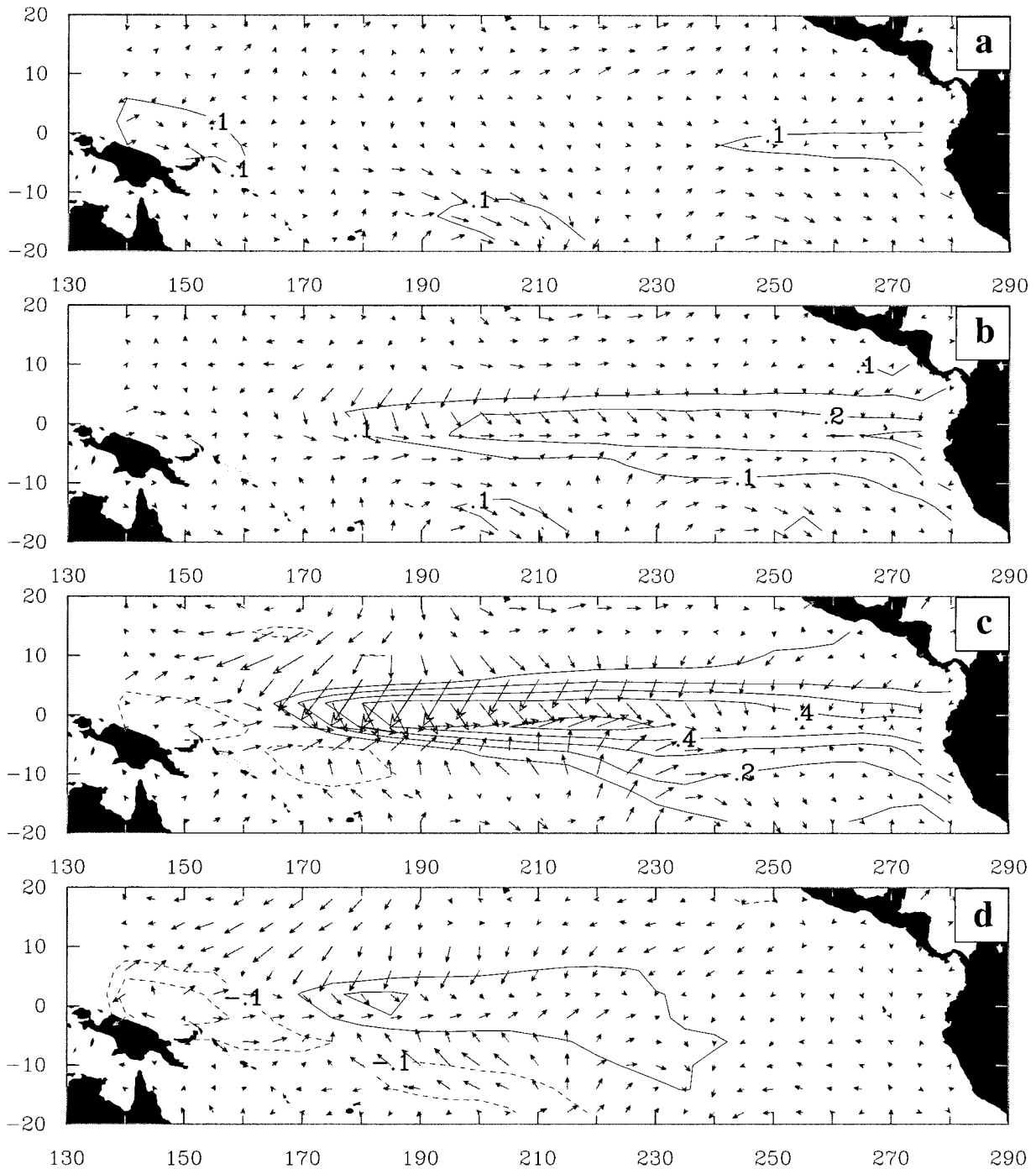


FIG. 6. SST and wind stress anomalies during the (a) onset, (b) growing, (c) mature, and (d) decaying stages of the warm phase of the leading oscillation mode obtained from the combined 5-variable M-SSA. Wind stress vectors are superimposed on SST contours. (a)–(d) The 17-, 20-, 27-, and 38-month time lag, respectively, in Fig. 5. Contour intervals are 0.1°C for SST. Zero contour lines are omitted.

develops, the zonal-mean anomalies gradually decay to completely vanish in the mature stage. As the warm phase decays (from months 28 to 37), negative ocean heat content anomalies build up and reach their largest magnitude at the onset of the cold phase. Thus, there is a 90° phase lag between the oscillations in zonal-

mean ocean heat content and SST anomalies at the equator. Figures 7b and 5a suggest that the variations of the zonal-mean ocean heat content anomalies at the equator are a key part of the phase-transition processes of the ENSO cycle. This is in general agreement with the recharge oscillator theory (Wyrski 1975; Zebiak and Cane

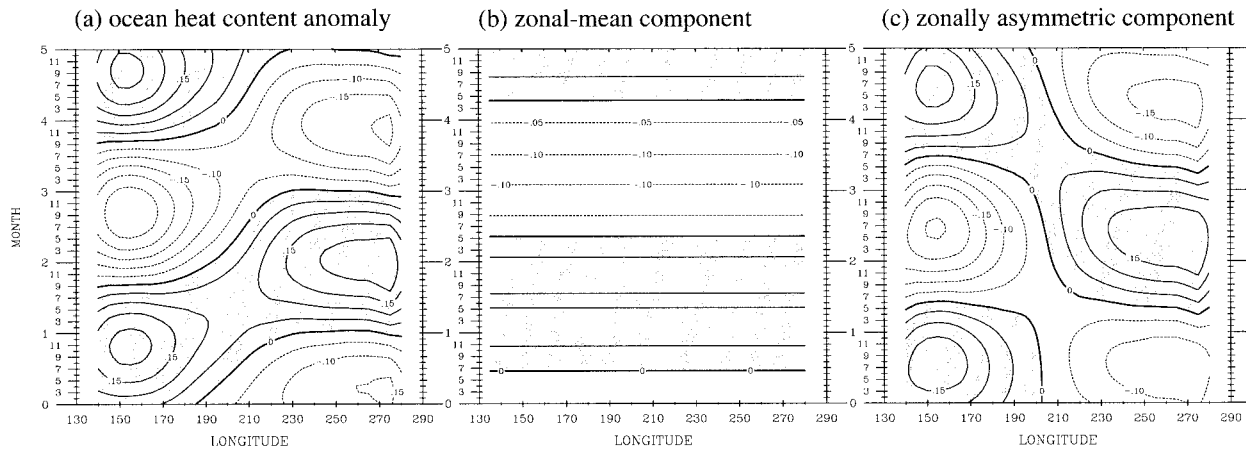


FIG. 7. Leading oscillatory mode of ocean heat content anomalies along the equator obtained from the combined 5-variable M-SSA: (a) the eigenvector, (b) its zonal-mean component, and (c) its zonally asymmetric component. The vertical coordinate spans the 61-month window used in M-SSA. Contour intervals are 0.05°C . Positive values are shaded.

1987; Jin 1997), which emphasizes the role of the buildup (i.e., charge) and release (i.e., discharge) of ocean heat content in the equatorial Pacific in the transitions between warm and cold ENSO events.

As for the zonally asymmetric component, Fig. 7c shows that it is characterized by the establishment of an east–west dipole along the equator. During the warm phase, ocean heat content increases in the eastern sector with a center around 100°W , and decreases in the western sector with a center around 155°E . During the cold phase, a similar east–west contrast with opposite polarity is established. Figures 5a and 7c clearly show that the amplitude of this east–west contrast increases from zero at the onset stages of both the warm and cold phases to reach maximum strength at the mature stages of both phases. This in-phase relationship with SST anomalies suggests that the zonally asymmetric component of the ocean heat content anomalies plays a key role in the growth of the ENSO cycle.

Our CGCM results on the roles of zonal-mean and zonally asymmetric components of ocean heat content anomalies at the equator during the ENSO cycle are consistent with the findings of Schneider et al. (1995). That study contrasted integrations of an ocean model in which wind stress forcing either was taken directly from observations or had exactly the same values but opposite time evolutions. At the equator, the two experiments produced similar east–west heat content contrasts, but very different zonal-mean heat content anomalies. The zonal contrast of ocean heat content anomalies is always in equilibrium with wind stress forcing and, therefore, does not depend on the history of wind stress forcing. On the other hand, the zonal-mean component carries the memory of atmospheric forcing.

The extent to which other parts of the tropical Pacific are involved in the buildup and release of zonal-mean ocean heat content anomalies at the equator has not been discussed in previous studies. To address this issue, we

examine the horizontal structures of ocean heat content anomalies in the Pacific between 20°S and 20°N . Figure 8 shows the eigenvector structures of the ocean heat content anomalies during various stages of the leading oscillatory M-SSA mode. Before the onset of the warm phase, the domain is characterized by ocean heat content anomalies that are positive around the equator and negative around 10°N (Fig. 8a). This north–south pattern changes gradually as the warm phase develops. First, positive heat content anomalies with large amplitude appear rapidly in the eastern equatorial Pacific (Figs. 8b, c). Negative anomalies later develop in the western equatorial Pacific (Fig. 8d). A strong east–west dipole of ocean heat content anomalies is established, which is strongest near the mature stage (Fig. 8e).

Figures 8c and 8d depict the establishment of a band of positive ocean heat content anomalies along 10°N starting during the mature stage of the warm phase. This 10°N band of anomalies strengthens further during the decaying phase (Figs. 8e–h). The establishment of this band in the central-to-western sector appears occurring simultaneously with the increase of negative ocean heat content anomalies in equatorial western Pacific. In the eastern sector, the 10°N band seems to be a “leakage” of the anomalies with the same sign that accumulated in the eastern sector during earlier stages. The leakage spreads first northward along the American coast and then westward along 10°N . There is no comparable development in the Southern Hemisphere. Near the end of the decaying phase, the pool of negative ocean heat content anomalies spreads rapidly to the entire equatorial band. At this stage, a south–north dipolar pattern of ocean heat content anomalies is reestablished between the equator and the 10°N with polarity opposite of that before the onset of the warm event (compare Figs. 8a and 8h).

The observational study of Zhang and Levitus (1997) reports a similar eastern boundary leakage into the

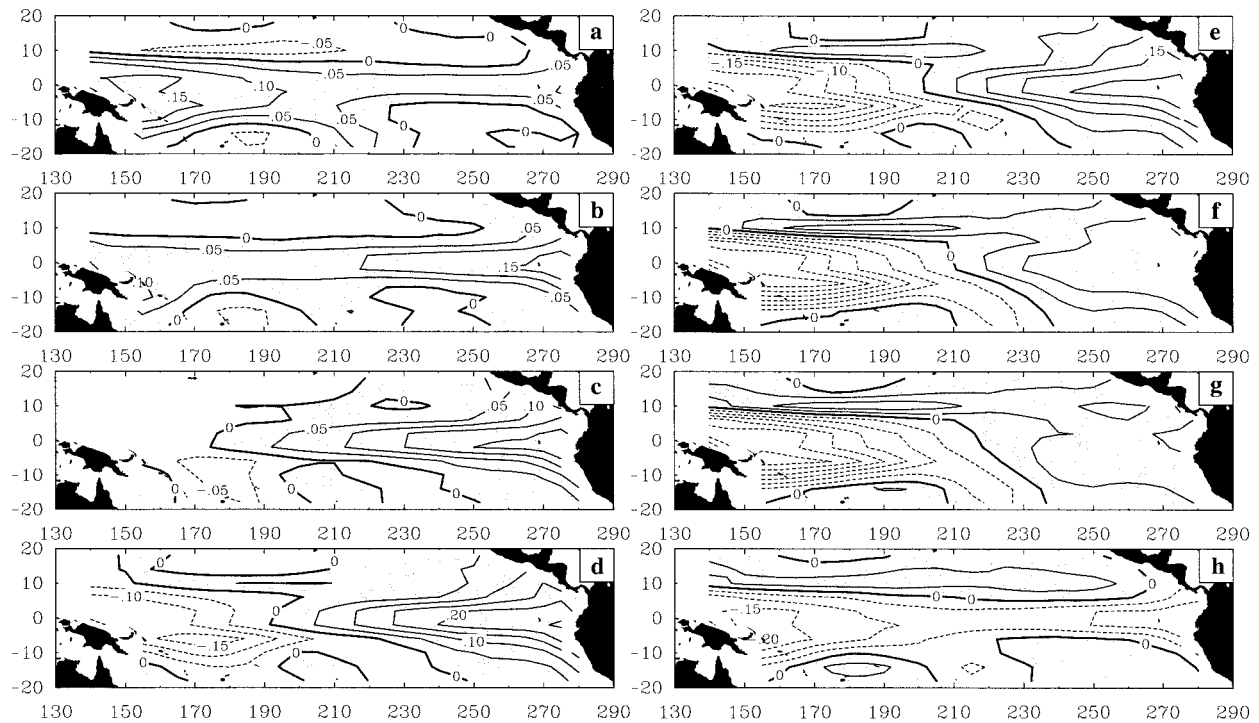


FIG. 8. Evolutions of ocean heat content anomalies obtained from the leading oscillatory mode of the combined 5-variable M-SSA. (a)–(d) The evolutions from the onset to growing stages of the warm SST phase and corresponding to the time lags 16, 19, 22, and 25, respectively, of the M-SSA mode. (e)–(h) The anomaly evolutions from the mature to decaying stages of the warm phase and corresponding to the time lags 28, 32, 35, and 41, respectively, of the M-SSA mode. Contour intervals are 0.05°C . Positive values are shaded.

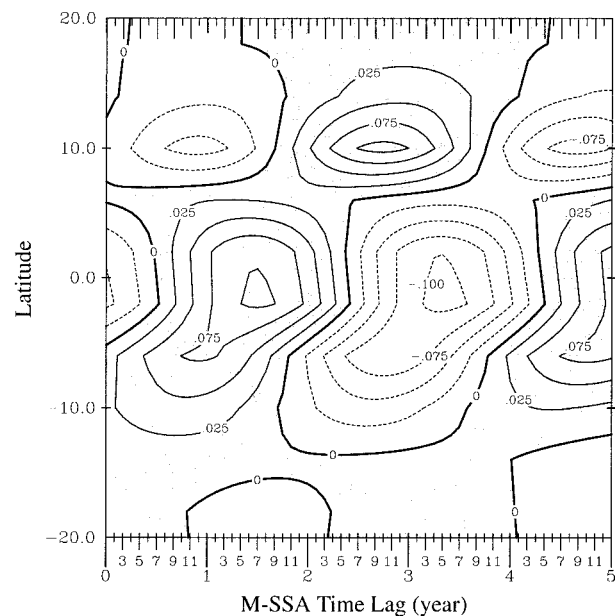


FIG. 9. Time evolution of the zonal-mean values of the eigenvector of ocean heat content anomalies from the leading M-SSA oscillatory mode. Contour intervals are 0.025°C . Positive values are shaded.

Northern Hemisphere. That study applies empirical orthogonal function (EOF) and correlation analyses to the upper-ocean temperature anomaly fields compiled by Levitus et al. (1994) from observations. Zhang and Levitus (1997) show that during El Niño (La Niña) events, positive (negative) equatorial temperature anomalies in the east move northward along the American coast and then propagate westward across the Pacific basin along 15°N . The similarity between their results and ours add credibility to the analysis strategy based on application of the M-SSA method and selection of the quasi-quadratic mode to represent ENSO.

The anticorrelation between ocean heat content at the equator and 10°N during the simulated ENSO cycle is further illustrated in Fig. 9. It is apparent that variations in zonal-mean ocean heat content anomalies in the equatorial band are approximately in phase with those south of 8°N and out of phase with those in a narrow band around 10°N . A similar north–south dipolar pattern of ocean heat content anomalies was obtained by Zebiak (1989) using a linear dynamical model forced with wind stress corresponding to the period of 1970–87. Zebiak (1989) found that ocean heat content is exchanged across the equator during the ENSO cycle. In his results, the largest differences between ocean heat content anomalies at 10°N and the equator occur approximately when SST anomalies switch from positive to negative (see his Fig. 4). Our results, obtained with a full CGCM,

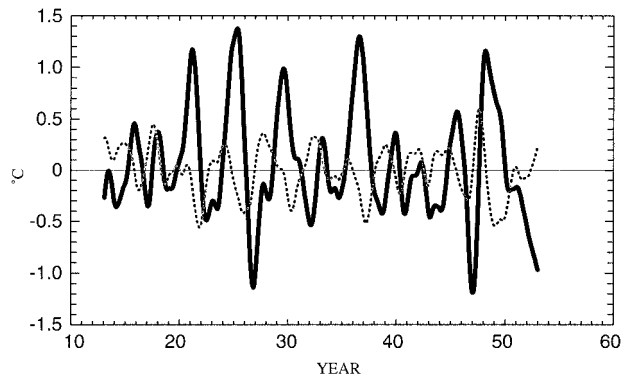


FIG. 10. Temporal variations of SST anomalies (solid line) in the central equatorial Pacific ($180^{\circ}\sim 120^{\circ}\text{W}$ and $2^{\circ}\text{S}\sim 2^{\circ}\text{N}$) and the difference (dashed line) between zonal-mean ocean heat content anomalies at the equator and at 10°N calculated from the CGCM simulation.

support his suggestion that the meridional displacement of ocean heat content is an integral component of the ENSO cycle.

To further examine the phase relationship between SST anomalies and the north–south dipole in ocean heat content anomalies, we plot in Fig. 10 the temporal variations of those two quantities. The SST time series represents values averaged in the region where SST anomalies have larger magnitudes ($180^{\circ}\sim 120^{\circ}\text{W}$ and $4^{\circ}\text{S}\sim 4^{\circ}\text{N}$). The north–south dipole of ocean heat content is represented by the difference between the zonal-mean anomalies at the equator and 10°N . Figure 10 shows that several warm/cold events in the simulation are preceded by a relative maximum/minimum in the north–south difference of ocean heat content anomalies. Furthermore, peaks in the latter time series have approximately the same magnitude, although SST anomalies during warm events can have significantly different magnitudes. Figure 10, therefore, suggests that the north–south ocean heat content contrast reaches a threshold near the onset of a warm/cold event. Figure 10 also shows that not every relative maximum/minimum value of the ocean heat content difference is followed by a warm/cold event. Reaching that threshold seems to be a necessary but not sufficient condition for ENSO onset.

6. Three-dimensional evolution of ocean temperature anomalies

In this section we examine the structure of temperature anomalies in the upper ocean during the ENSO cycle and their evolutions. A three-dimensional oscillatory mode of ocean temperature anomalies is obtained by applying the M-SSA method to the low-pass filtered anomalies in the upper 300 m of the ocean between 20°S and 20°N . This mode explains about 37% of the total variance. Figure 11 displays longitude–depth cross sections at the equator of the corresponding eigenvector for the preonset, onset, growth, mature, and decay stages of the warm phase of the cycle. Figure 12 shows the

corresponding latitude–depth cross sections of zonal-mean anomalies.

Figure 11a shows that before the onset of the warm phase of ENSO, a large pool of positive temperature anomalies already exists in the western equatorial Pacific at a depth of about 110 m. As mentioned in section 5, the preonset stage is characterized by a gradual increase of zonal-mean heat content anomalies at the equator (see Fig. 7b). Therefore, Fig. 11 indicates that the dominant contribution to this increase comes from the subsurface in the equatorial western Pacific. As the onset approaches, the subsurface temperature anomalies extend eastward and upward toward the surface of the eastern equatorial Pacific (Fig. 11b). This extension is approximately along the long-term mean slope of the equatorial thermocline (Fig. 11f). Similar eastward migration was also reported in an earlier CGCM study (Nagai et al. 1990). Figures 12a and b show that zonal-mean ocean temperature anomalies during these two stages are mostly confined to the equator and are characterized by a slow upward movement from -110 m to the surface. The anomalies eventually surface in the equatorial eastern Pacific, which marks the onset of a warm event. These simulated characteristics of ocean temperature anomalies in the preonset stages of the warm ENSO phase are strikingly similar to those observed by the Tropical Oceans and Global Atmosphere Tropical Atmosphere–Ocean Array for the 1997–98 El Niño event (Trenberth 1998; McPhaden 1999). The observations show that a pool of subsurface temperature anomalies was present several months before the onset of the 1997–98 warm ENSO event. Furthermore, the observed subsurface pool was also centered approximately 100 m below the surface.

In the growth stage, Fig. 11c shows a very rapid and complete shift along the equator of positive temperature anomalies from the western subsurface to the eastern surface, and a westward extension of SST anomalies on the surface (Fig. 11c). Later in the growth stage and through the decay stage, a pool of negative anomalies begins to build up in the west at a depth of about 110 m (Figs. 11d and 11e). Simultaneously, the positive temperature anomalies near the surface eastern equatorial Pacific start expanding away from the equator (Figs. 12d and 12e). As a result, the positive anomalies in the upper part of the equatorial Pacific decrease gradually, while the negative anomalies in the lower part of the upper ocean continue to grow. This tendency continues until the decay stage of the warm ENSO phase. The zonal-mean ocean heat content anomalies at the equator, therefore, must decrease from positive to negative values from the growth stage to the decay stage. This is consistent with the variations in the zonal-mean component of ocean heat content anomalies seen in Fig. 7b. A notable feature in Figs. 12c–e is that equatorial ocean temperature anomalies expand only into the Northern Hemisphere, particularly toward 10°N . At 10°N , the

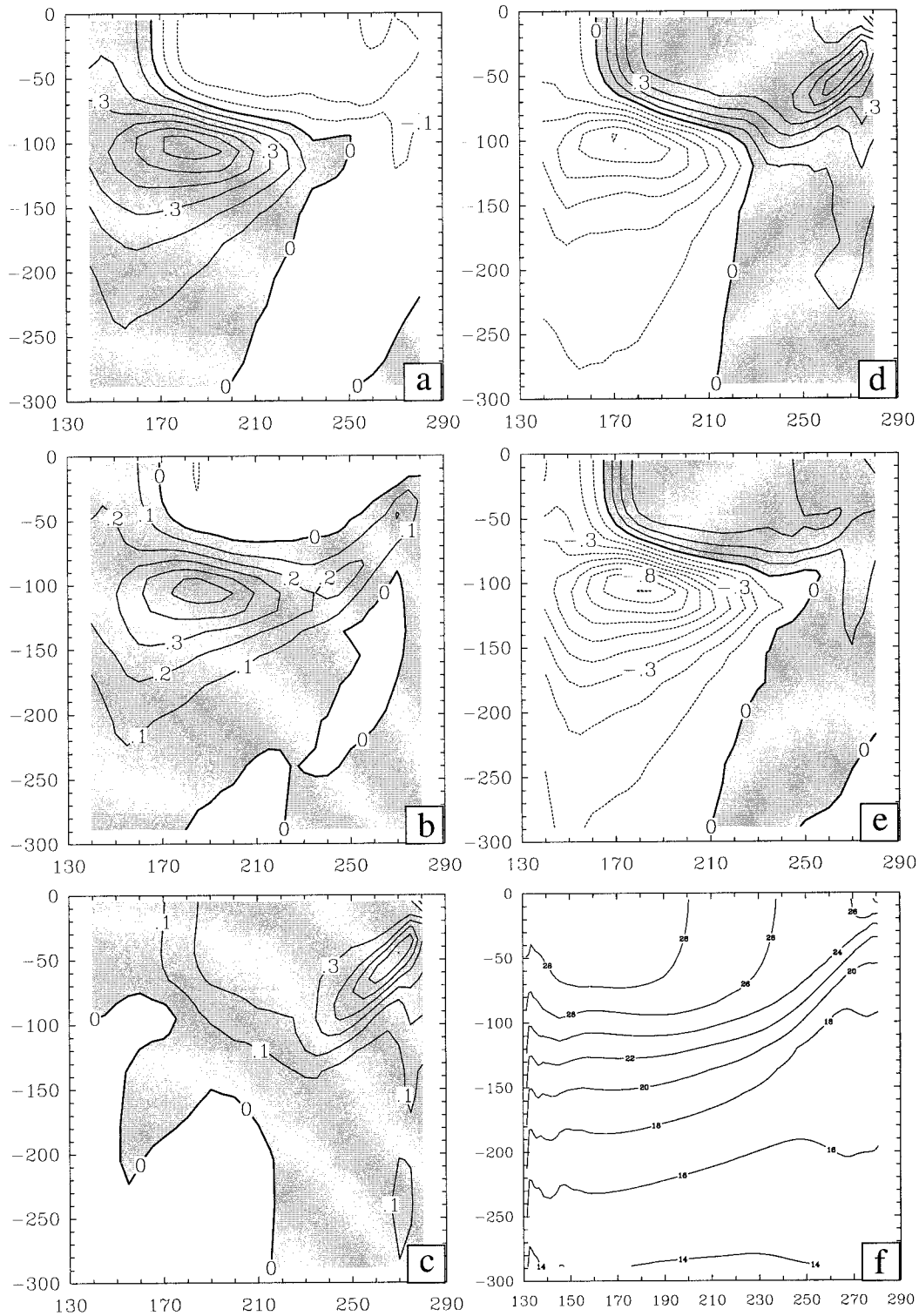


FIG. 11. Longitude–depth plots of ocean temperature anomalies at the equator during various stages of the leading oscillation mode. The mode is obtained by applying the M-SSA to the ocean temperature anomalies from 20°S to 20°N, from 130°E to 70°W, and from surface to –300 m. (a)–(e) The decay stage of the cold phase (10-month lag) and the onset (15-month lag), growing (21-month lag), mature (27-month lag), and decaying (33-month lag) stages, respectively, of the warm phase. (f) The long-term mean isotherms at the equator. Contour intervals are 0.10°C for (a)–(e) and 2°C for (f). Positive anomalies are shaded.

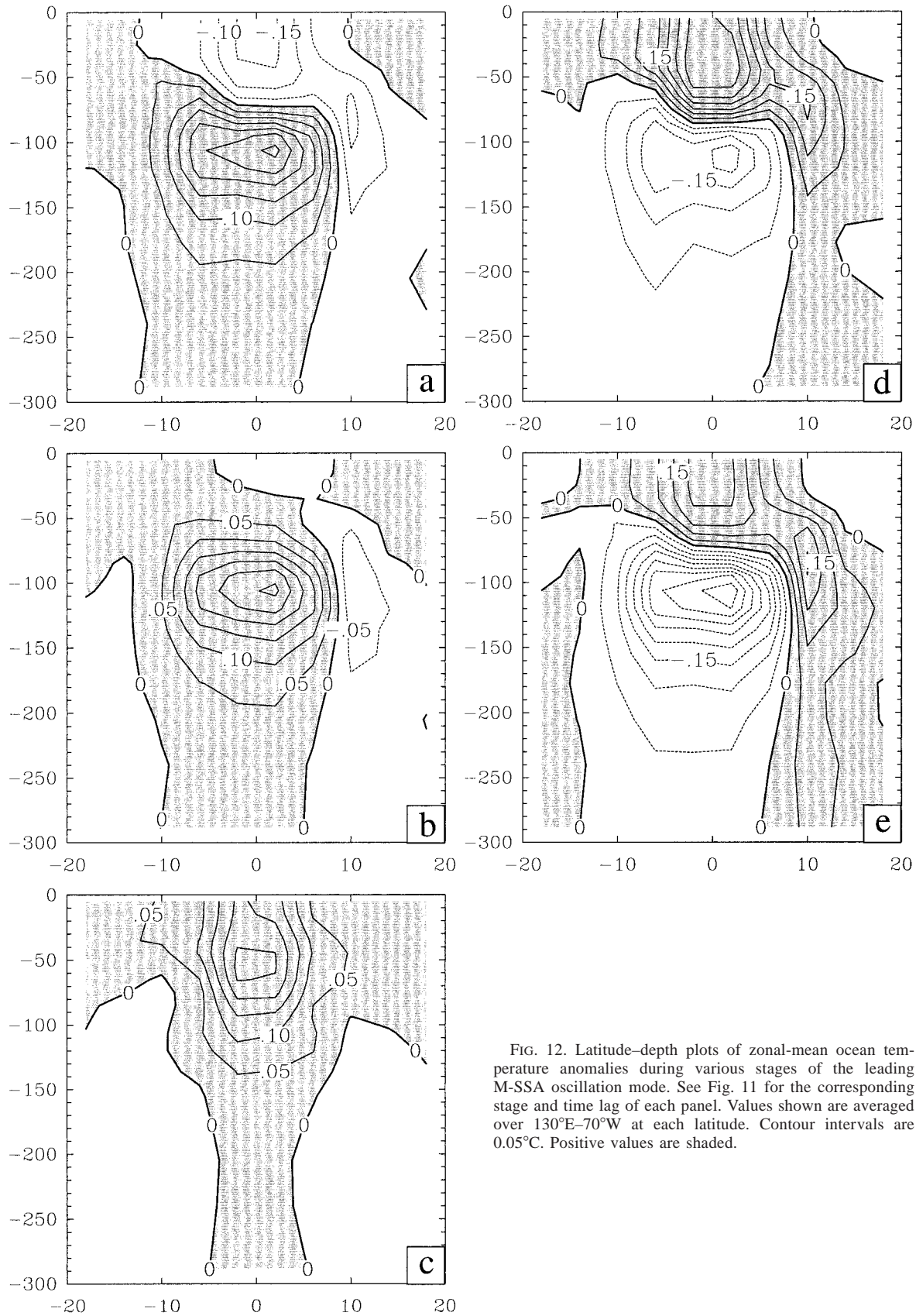


FIG. 12. Latitude–depth plots of zonal-mean ocean temperature anomalies during various stages of the leading M-SSA oscillation mode. See Fig. 11 for the corresponding stage and time lag of each panel. Values shown are averaged over 130°E–70°W at each latitude. Contour intervals are 0.05°C. Positive values are shaded.

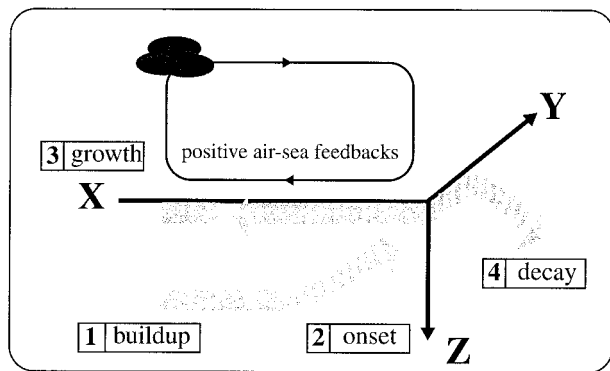


FIG. 13. A schematic of the four major movements of ocean temperature anomalies in the Pacific during the ENSO cycle. These processes include 1) buildup of a pool of surface temperature anomalies in the equatorial western Pacific, 2) a slow eastward and upward extension of the temperature anomalies from the western subsurface pool toward the surface of equatorial eastern Pacific during the onset stage, 3) a rapid amplification and slow westward expansion of SST anomalies on the ocean surface during the growing stage, and 4) the gradual northward and downward spread of temperature anomalies from the eastern equatorial Pacific toward the subsurface at 10°N during the decaying stage. The positive air-sea feedback is considered part of the growing stage.

anomalies move across the basin and return to the western sector at a depth of about -110 m.

Based on the three-dimensional analysis presented in this section, we can describe the ENSO cycle as consisting of four major features in the ocean temperature anomalies (see Fig. 13): 1) a buildup in the subsurface of the western equatorial Pacific during the preonset stage, 2) a spread from the western subsurface to the eastern surface along the equator during the onset stage, 3) a zonal extension and amplification at the surface during the growing stage, and 4) a northward and downward spread during the decaying stage. These results suggest that both the equatorial and off-equatorial Pacific are involved in the ENSO cycle. They also suggest that the leakage of equatorial ocean heat content anomalies along the eastern basin is an integral part of the oscillation in the zonal-mean ocean heat content at the equator. This process, therefore, cooperates with western boundary reflection and Sverdrup transport in providing the negative feedback required for the oscillation.

7. Oceanic heat budget analysis

To contrast the relative contribution of different processes to the evolution of ocean temperature anomalies during the ENSO cycle, we analyze the various terms in the OGCM's temperature equation. This can be written as

$$\frac{\partial T}{\partial t} = -V \cdot \nabla T - w \frac{\partial T}{\partial z} + \frac{1}{\rho C_p} \frac{\partial F}{\partial z} + \frac{\partial}{\partial z} \left(K_H \frac{\partial T}{\partial z} \right), \quad (1)$$

where T is ocean temperature, t is time, V is horizontal velocity, w is vertical velocity, z is the vertical coor-

dinate, F is the vertical heat flux, ρ is density, and C_p is the specific heat of water. K_H is the vertical diffusion coefficient, whose value is determined by the Mellor-Yamada level $2\frac{1}{2}$ turbulence closure scheme (Mellor and Yamada 1982). The terms on the right-hand side of (1) represent the horizontal advection, vertical advection, heating due to surface heat flux, and turbulent vertical diffusion. The temperature changes due to horizontal diffusion and convective adjustment are not considered but are believed to be small.

Figures 11 and 12 suggest that for analyses of the temperature evolution during the ENSO cycle the upper ocean can be approximated by two layers with an interface at around 60–70 m deep. The vertical-mean temperatures in these layers represent the surface and subsurface thermal anomalies. Therefore, we examine separately the vertically averaged temperature budget in the top six model layers (surface–60 m deep) and the following five model layers (80–145 m deep). The corresponding equations can be written in the following way:

$$\begin{aligned} \left(\frac{\partial T}{\partial t} \right)_{\text{upper}} &= \frac{1}{\Delta z_{\text{upper}}} \int_{z_1}^0 \left(-u \frac{\partial T}{\partial x} \right) dz \\ &+ \frac{1}{\Delta z_{\text{upper}}} \int_{z_1}^0 \left(-v \frac{\partial T}{\partial y} \right) dz \\ &+ \frac{1}{\Delta z_{\text{upper}}} \int_{z_1}^0 \left(-w \frac{\partial T}{\partial z} \right) dz + \frac{1}{\Delta z_1} \frac{F}{\rho C_p} \\ &- \frac{1}{\Delta z_1} \left(K_H \frac{\partial T}{\partial z} \right)_{z_1}, \end{aligned} \quad (2)$$

$$\begin{aligned} \left(\frac{\partial T}{\partial t} \right)_{\text{lower}} &= \frac{1}{\Delta z_{\text{lower}}} \int_{z_3}^{z_2} \left(-u \frac{\partial T}{\partial x} \right) dz \\ &+ \frac{1}{\Delta z_{\text{lower}}} \int_{z_3}^{z_2} \left(-v \frac{\partial T}{\partial y} \right) dz \\ &+ \frac{1}{\Delta z_{\text{lower}}} \left[\int_{z_3}^{z_2} \left(-w \frac{\partial T}{\partial z} \right) dz \right] \\ &+ \frac{1}{\Delta z_{\text{lower}}} \left(K_H \frac{\partial T}{\partial z} \right) \Big|_{z_3}^{z_2}, \end{aligned} \quad (3)$$

where $Z_1 = -60$ m, $Z_2 = -80$ m, $Z_3 = -145$ m, $\Delta Z_{\text{upper}} = 60$ m, and $\Delta Z_{\text{lower}} = Z_2 - Z_3 = 65$ m. We start by computing all terms in (2) and (3) based on the three-day-mean u , v , w , T , and $K_H \partial T / \partial z$ in the model's history files. Next we remove the annual cycle of each term, use a low-pass filter to remove variations with time-scales shorter than 1 yr, and apply the M-SSA method. The leading pair of M-SSA modes together explains 33% of the total variance of $(\partial T / \partial t)_{\text{upper}}$ and $(\partial T / \partial t)_{\text{lower}}$,

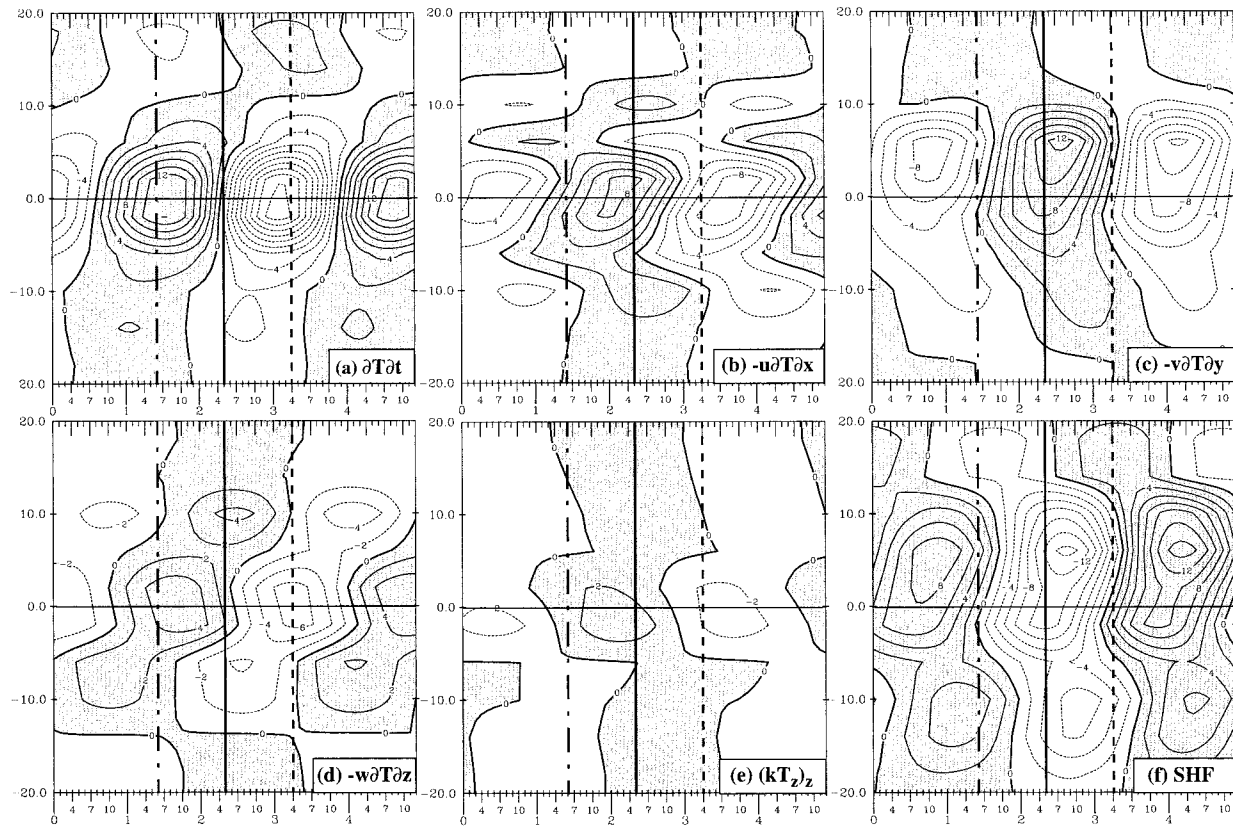


FIG. 14. Latitude–time structures of the budget terms for the upper-ocean layer during the simulated ENSO cycle. The structures are obtained from M-SSA analysis: (a) the time tendency term, (b) the zonal advection term, (c) the meridional advection term, (d) the vertical advection term, (e) the vertical diffusion term, and (f) the surface heat flux heating term. The onset, mature, and termination stage of the warm phase are indicated, respectively, by dot-dashed, solid, and dashed lines. Values shown are zonal averages and are amplified by 10 000. Contour intervals are $2^{\circ}\text{C day}^{-1}$. Positive values are shaded.

and a power spectrum of the PCs gives a dominant period of about 48 months.

a. Upper ocean layer

Figure 14 presents the zonally averaged structures of the eigenvectors corresponding to the first M-SSA mode for the upper ocean layer. The following discussions focus on the warm phase, since the cold phase can be approximately obtained by sign reversal. Figures in this section of the paper label the onset, mature, and termination times of the warm phase by dot-dashed, solid, and short-dashed lines, respectively.

Figure 14a shows that the largest temperature changes in the upper layer occur at the equator. Figure 14d shows that the vertical advection term is the only rhs term that has a temporal behavior similar to the temperature tendency term, although with a slight phase lag. The zonal advection term lags the tendency term by about 7 months (Fig. 14b). Thus, the contribution to temperature changes by zonal advection is strongest toward the end of the growing period. The meridional advection and surface heat flux terms are almost 90° out of phase with the tendency term. The surface heat flux term provides

a negative contribution to the temperature tendency during the warm phase, while the meridional advection term provides a positive contribution. Both terms have their largest values in the Northern Hemisphere. At the equator, these terms have larger magnitudes than the other budget terms, but they tend to cancel each other due to the difference in phase. The contribution of the vertical diffusion term is very small and can be neglected for the upper ocean layer. Therefore, Fig. 14 suggests that vertical and zonal advective processes are the main processes that drive the changes of zonal-mean temperature in the upper ocean layer. Surface heat flux and meridional advection respond to the warm phase development but their combined effects on zonal-mean temperature changes are small.

Figure 15 displays the horizontal structures of terms in the temperature equation for the upper ocean layer at the onset and mature times of the warm phase. At the onset, most ocean temperature changes occur in the eastern and central sectors (Fig. 15a) with the largest warming along the South American coast. The major contribution to this warming is given by the vertical advection term (Fig. 15d). This can be associated either

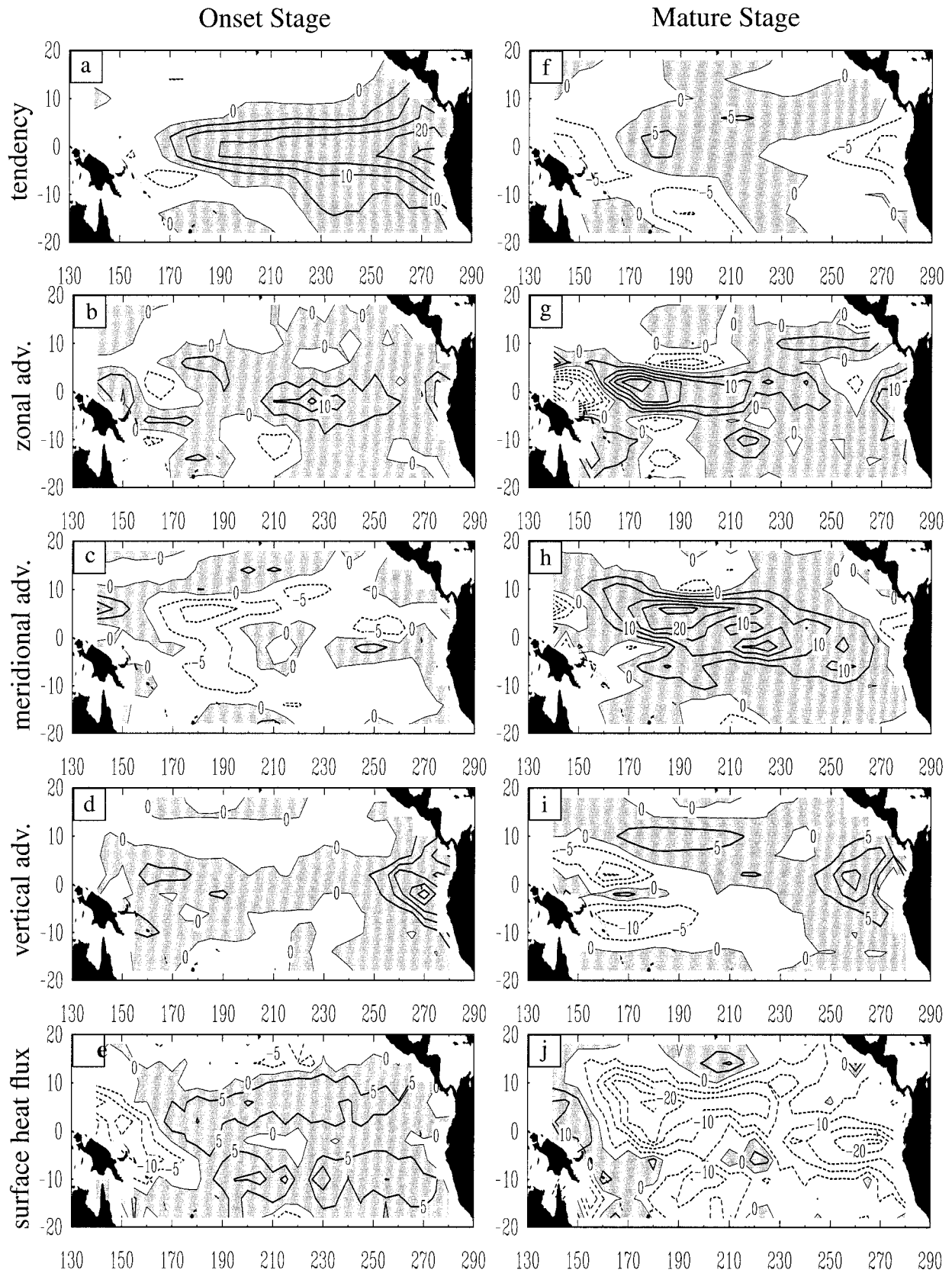


FIG. 15. Horizontal structures of the temperature budget terms for the upper ocean layer. The left panels show the structures at the onset stage of the warm phase, and the right panels are those for the mature stage. Values shown are amplified by 10 000. Contour intervals are $5^{\circ}\text{C day}^{-1}$. Positive values are shaded.

with a weakening of the coastal upwelling or with a deepening of the thermocline in view of

$$\left(-w\frac{\partial T}{\partial z}\right)' \approx -w'\left(\frac{\partial \bar{T}}{\partial z}\right) - \bar{w}\left(\frac{\partial T}{\partial z}\right)', \quad (4)$$

where primes indicate anomaly and bar indicate mean state. Since surface wind stress anomalies are weak during the onset, the variation in the vertical advection term is likely caused by the deepening of the thermocline, that is, $-\bar{w}(\partial T/\partial z)'$. Zonal advection contributes to the warming tendency in the eastern and central sectors by advecting positive SST anomalies westward from the coastal region (Fig. 15b). Surface heat flux also contributes to the warming tendency in the central and western sectors (Fig. 15e), but this contribution is largest off the equator in both the Northern and Southern Hemisphere. At the equator, values are small except for the western sector, where they are negative. The meridional advection term also has largest magnitudes off the equator, but these are mostly confined to the Northern Hemisphere. The vertical and zonal advection terms continue to dominate the temperature tendency throughout the growing period (not shown), but their magnitudes decrease as the mature stage approaches.

At the mature stage, the warming tendency continues in the central-to-western sector but a cooling tendency appears in the eastern sector (Fig. 15f) where positive SST anomalies stop growing. Figure 15j shows that the surface heat flux term is the major contributor to this cooling in the eastern sector. The meridional advection term also contributes to the cooling tendency along the south-to-central American coast. This term basically reflects the eastern boundary leakage to the Northern Hemisphere discussed in sections 5 and 6. The zonal advection term is the sole contributor to the continuous warming tendency in the central-to-western sector at this time (Fig. 15g). The center of large zonal advection is always located west of the SST anomaly center and propagates westward as the warm phase develops. This behavior of advection can be described by an expression that takes into account the wind-forced ocean currents, that is, $-u'(\partial \bar{T}/\partial x)$, in a way consistent with the slow SST theory (Neelin 1991; Neelin and Jin 1993; Jin and Neelin 1993a,b). As the warm phase starts decaying, a cooling tendency spreads from the eastern to the central-to-western sector (not shown). During this period, the vertical advection is larger than the surface heat flux and meridional advection terms and determines the cooling tendency in the eastern sector until the onset of the following cold phase.

In discussing Fig. 14 we already mentioned that the meridional advection and surface heat flux terms have largest magnitudes around 6°N, not at the equator. Strong trade wind anomalies also develop during the ENSO cycle around that latitude (see Fig. 6). This coincidence suggests that surface wind stress may play an important role in determining the latitudinal structure

of these two terms. To address this point, we display in Fig. 16 the latitude-time structures of both components of surface wind stress anomalies and wind stress magnitude obtained from the combined 5-variables M-SSA analysis discussed in section 4. It is apparent that both components of surface wind stress, as well as the wind stress magnitude, have their largest values around 6°N. The latitudinal structure of the wind stress magnitude in the Northern Hemisphere is very similar to that of the surface heat flux term (compare Figs. 16c and 14f). This similarity suggests that wind-controlled surface evaporation processes are dominant in the response to ENSO of surface heat flux around 6°N.

The off-equatorial center of the meridional advection term in the Northern Hemisphere can also be linked to the trade wind anomalies distribution via Ekman transports. According to Fig. 16, there are strong easterly wind stress anomalies between 4° and 20°N with a local maximum around 6°N during the growing period of the warm phase. A northward Ekman transport and positive meridional advection can, therefore, be expected in this region. Southward of 4°S, the zonal-mean values of zonal wind stress anomalies are positive. However, only wind stress anomalies in the *western part* of the southern Pacific are negative with small values (see Fig. 6c). Therefore, meridional temperature advection associated with Ekman transports in this part of the South Pacific has to be positive and small. Near the equator, Ekman transports are weak. The large values of the meridional temperature advection at this latitude are located in the eastern sector (see Fig. 15h), where trade wind anomalies are small. Therefore, the advection here is likely related to the southward anomalous current induced by the weakening of upwelling, which brings the warmer mean SSTs into the equator by a term of the form: $-v'(\partial \bar{T}/\partial y)$. As a result, the meridional advection term is positive between 10°S and 10°N and has a maximum center at 6°N. The large cancellation between the surface heat flux and meridional advection terms, therefore, is rooted in their mutual dependence on trade wind anomalies in the subtropical Pacific.

We can also use Ekman transport arguments to understand the latitudinal structure of the vertical advection term. Vectors in Fig. 16a represent the direction and magnitude of Ekman transport at the mature stage of the warm phase based on the zonal wind stress anomalies in the western sector. Convergence of the Ekman transport at 10°N is consistent with a deepening of the local thermocline, while divergence near 2°N and 6°S is consistent with the shoaling of the thermocline in these regions. Figure 15i shows that at the mature stage there is a positive vertical temperature advection band centered at 10°N and bands of negative vertical temperature advection centered at 2°N and 6°S. This figure also suggests that the zonal-mean values of the vertical advection term off the equator are dominated by those in the western sector. Here, vertical advection is primarily determined by wind stress forcing, and therefore

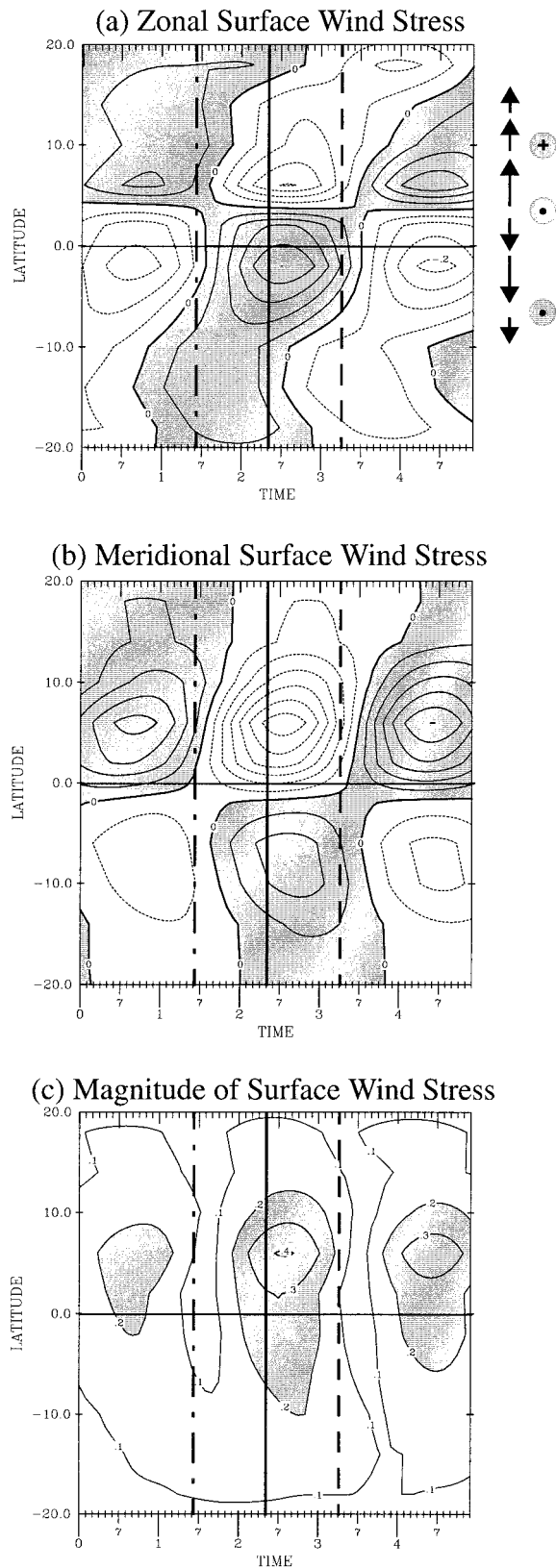


FIG. 16. The time–latitude structures of the eigenvectors of (a) the zonal and (b) meridional components of surface wind stress obtained

has a 90° phase lag with the tendency term. In the equatorial band, the zonal mean of the vertical advection term is dominated by advection processes in the eastern sector. In this sector, vertical advection is not determined by wind stress forcing and is in phase with the tendency term. This is consistent with the latitudinal structure of the vertical advection term shown in Fig. 14d.

b. Lower ocean layer

Figure 17 displays the zonally averaged structures of the eigenvectors corresponding to the first M-SSA mode of the temperature budget equation for the lower ocean layer. Figure 17a shows that there are centers of large temperature changes at the equator and near 10°N . This latitudinal structure is similar to the north–south dipole pattern in ocean heat content anomalies (see Figs. 8 and 9). It appears, therefore, that variations of the north–south dipole pattern are dominated by temperature variations in the lower ocean layer. At both the equator and 10°N , temperature tendencies are largest during the mature stage. The meridional advection, vertical diffusion, and vertical advection terms have comparable magnitudes and similar phases at the equator and are all important contributors to the tendency term. The temperature tendency near 10°N , on the other hand, is dominated by vertical advection. During the mature stage, the vertical advection term has local maxima at 6°S , 2°N , and 10°N (Fig. 17d). These are the same latitudes where the upper ocean layer produces strongest vertical advection in the same stage due to Ekman pumping (see Fig. 15i). Therefore, the vertical advection term in the lower layer also reflects the deepening/shoaling of the thermocline induced by Ekman transports.

Figure 18 displays the horizontal structures of the terms in the temperature budget for the lower ocean layer. The panels correspond to the onset time for the zonal advection term and to the mature time for all other terms. Figure 18a shows that the strongest cooling tendencies at the equator occur in the central and western sectors. The vertical advection term is the principal contributor to the cooling tendency in the western sector (Fig. 18c), while the meridional advection term is the principal contributor in the central sector (Fig. 18b). The latter term is related to the Sverdrup transport forced by the curl of surface wind stress anomalies. The negative gradient of zonal wind stress anomalies between the equator and 6°N (see Fig. 16a) implies a northward

←

from the combined 5-variable M-SSA. (c) The magnitude of the surface wind stress. Vectors along (a) represent the direction and magnitude of Ekman transport at the mature stage of the warm phase based on the zonal wind stress anomalies in the western sector. The coordinate is the 61-month window lag used in M-SSA. Values shown are amplified by 10. Contour intervals are (a), (b) 0.05 dyn cm^{-2} and (c) 0.1 dyn cm^{-2} . Positive values in (a) and (b) are shaded; in (c), magnitudes larger than 0.2 are shaded.

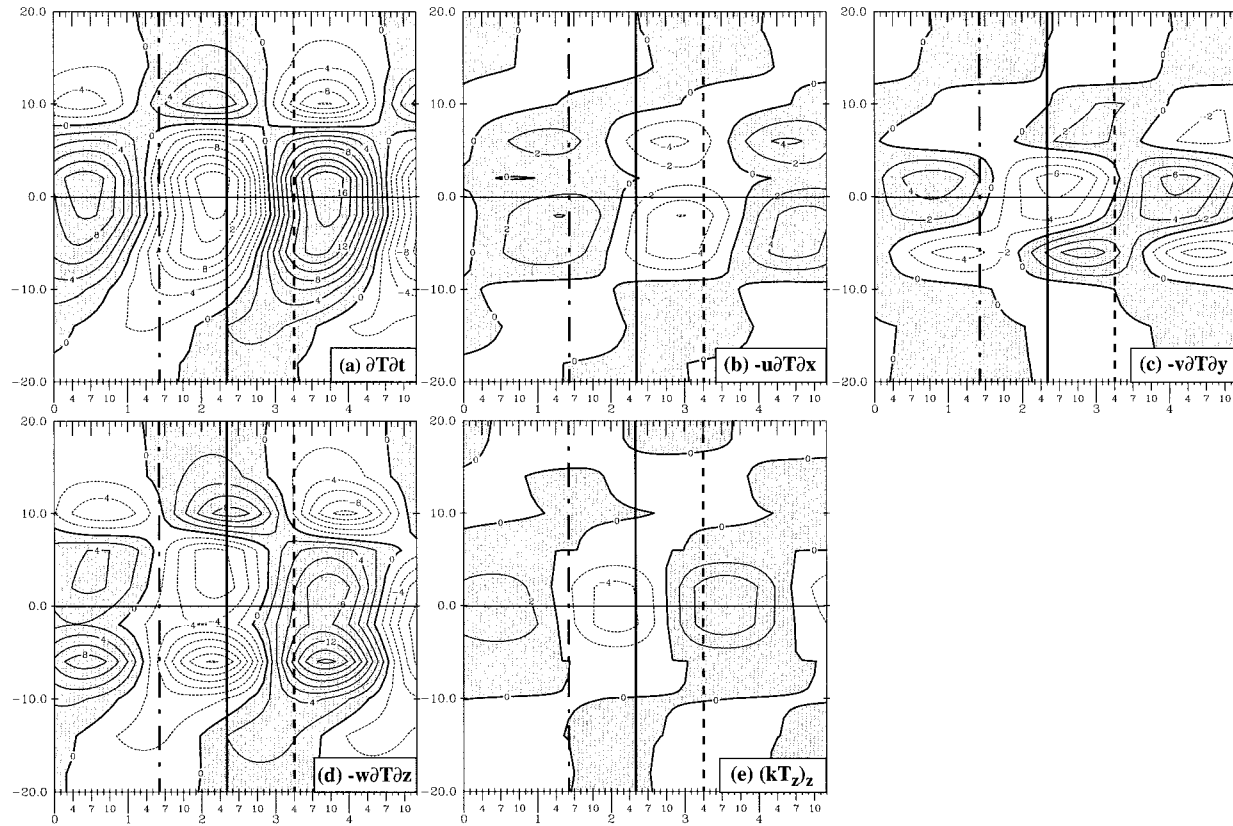


FIG. 17. Same as Fig. 14 but for the lower ocean layer and with the surface heat flux heating term omitted

Sverdrup flow at the mature stage of the warm phase. The negative gradient between the equator and 2°S implies a southward flow. Both flows can advect warmer subsurface temperatures away from the equator and result in negative meridional temperature advection.

The vertical diffusion term also contributes to the cooling tendency in the central Pacific (Fig. 18d). The magnitude of the contribution is about 50% of that from the meridional advection term. Figure 18e displays the structure of the zonal advection term at the onset stage of the warm phase. At this stage, the zonal advection is positive in most of the equatorial band. This term basically reflects the eastward extension of the positive subsurface temperature anomalies (Fig. 11b). Therefore, this is the only budget term in the lower ocean layer that does not act to build up the subsurface temperature pool, but instead acts to bring these anomalies to the ocean surface in the eastern sector. Its role, therefore, is to provide the oceanic part of the “triggering” process for ENSO.

In summary, we can provide the following description of the temperature changes in the upper and lower ocean layers during the ENSO cycle. Prior to the warm phase, vertical advection warms the upper ocean in the far eastern sector and leads to the onset of the warm phase. Zonal advection thereafter expands SST anomalies westward toward the central Pacific. Surface heat flux

tends to reduce those anomalies, but its effects are largely canceled out by warming associated with meridional advection. In the eastern sector, however, surface heat flux eventually stops the growth of SST anomalies. Surface wind responses in the western Pacific induce meridional Ekman transport in the upper ocean layer. Convergence and divergence of those transports lead to a deepening of the thermocline at 10°N and a shoaling of the thermocline at the equator, respectively. The latter process produces the negative SST anomalies in the western Pacific during the warm phase of ENSO. These downward movements of thermocline on both sides of the equator reach the lower ocean layer and produce strong cooling tendencies there. Trade wind anomalies also induce Sverdrup transport in the lower layer and result in cold meridional advection in the central sector of the equatorial Pacific. The strong cooling produced by surface heat fluxes is also partially diffused down to the lower layer and contributes to cooling there. As a result of the vertical advection, meridional advection, and vertical flux convergence processes, a pool of negative temperature anomalies is built up in the lower layer. Later, zonal advection brings those anomalies eastward to the eastern sector. As this happens, vertical advection begins cooling the upper ocean, leading to the onset of the cold phase.

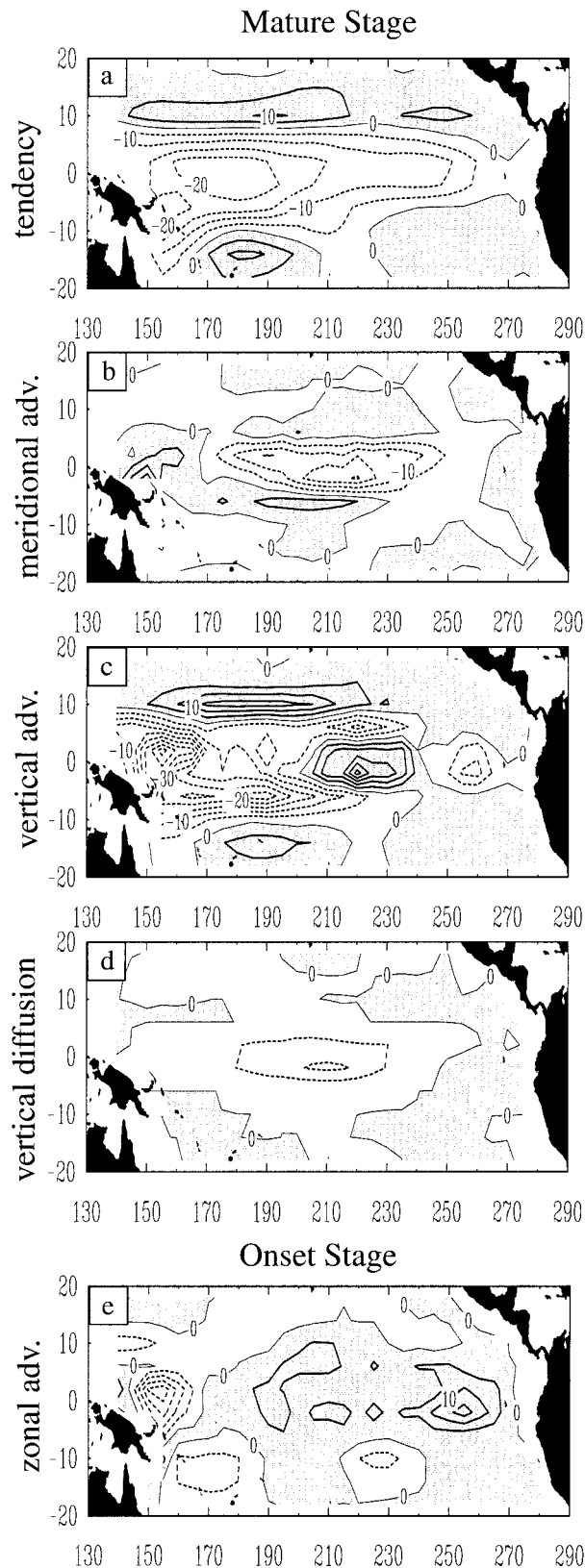


FIG. 18. Horizontal structures of the temperature budget terms for the lower ocean layer. (a)–(d) The structures at the mature stage of

8. Discussion and conclusions

This study examined the ENSO cycle produced by a recent version of the UCLA CGCM, in which the OGCM domain is restricted to the tropical Pacific. The atmospheric component of the CGCM incorporates extensive revisions, which have greatly alleviated systematic errors of previous model versions and resulted in an improved simulation of the interannual variability. In particular, warm and cold SST events are produced by the model with realistic frequency and amplitude. The simulated results, therefore, offer an opportunity to better understand the dynamical processes that determine the origin and evolution of ENSO. Analyses based on the M-SSA method provided a detailed description of the structure and evolution of atmospheric and oceanic anomalies associated with a quasi-quadrennial oscillation that we identified with ENSO. This was found to be characterized by predominantly standing oscillations of SST in the eastern Pacific, almost simultaneous zonal wind stress anomalies to the west of the SST anomalies, and preceding thermocline anomalies near the eastern edge of the basin.

In terms of the ocean heat content, which was defined as the vertically averaged temperature in the upper 300 m of the ocean, the simulated ENSO cycle is characterized by a zonal oscillation between the western and eastern equatorial sectors and a meridional oscillation between the equator and 10°N. The zonal oscillation appears related to the growth/decay processes of ENSO. The meridional oscillation has a 90° phase lag with that in SST, and therefore appears related to the phase-transition processes of the cycle. Our analyses suggest that the amplitude of this oscillation must research a threshold value for ENSO onset.

An analysis of ocean temperature anomalies in the upper 300 m of the ocean revealed that the ENSO cycle is characterized by four major features in the behavior of ocean temperature anomalies. First, anomalies build up in the western equatorial Pacific under the surface during the preonset stage. Second, they spread from the western subsurface to the eastern surface during the onset stage. Third, surface anomalies spread westward and amplified during the growth stage. Last, anomalies spread northward and downward to the Northern Hemisphere during the decay stage.

Our analyses of the ocean temperature budget for the upper ocean show that the primary contributors to the buildup of subsurface temperature anomalies are vertical advection in the western sector and meridional advection in the central sector. The former process is associated with vertical displacements of the thermocline and is an important element of the delayed oscillator

←

the warm phase; (e) the structure at the onset stage. Values shown are amplified by 10 000. Contour intervals are 5°C day⁻¹. Positive values are shaded.

theory. The latter process is associated with Sverdrup imbalance between trade wind and thermocline and is emphasized by recharge oscillator theory as the primary charge–discharge process. These results, therefore, indicate that both vertical and meridional temperature advections play key roles in producing subsurface ocean memory for the phase transitions of the ENSO cycle.

Acknowledgments. The authors benefited from discussions with A. Arakawa, G. S. H. Philander, A. W. Robertson, and J. D. Neelin during the course of this study. Comments from D. S. Battisti, F.-F. Jin, M. J. McPhaden, J. C. McWilliams, M. J. Suarez, and S. E. Zebiak are appreciated. A. Robertson provided a software package for the M-SSA analysis. This study was supported by NOAA GOALS Grant NA66GP0121 and by UC Campus Laboratory Collaboration Program. Model integrations were performed at the San Diego Supercomputer Center (SDSC) and the Climate Simulation Laboratory (CSL) at NCAR.

REFERENCES

- Alexander, R. C., and R. L. Mobley, 1976: Monthly average sea-surface temperatures and ice pack limits on a 1×1 global grid. *Mon. Wea. Rev.*, **104**, 143–148.
- Arakawa, A., and W. H. Schubert, 1974: Interaction of a cumulus cloud ensemble with the large-scale environment, Part I. *J. Atmos. Sci.*, **31**, 674–701.
- Battisti, D. S., and A. C. Hirst, 1989: Interannual variability in the tropical atmosphere–ocean system: Influence of the basic state, ocean geometry, and nonlinearity. *J. Atmos. Sci.*, **46**, 1687–1712.
- Bjerknes, J., 1969: Atmospheric teleconnections from the equatorial Pacific. *Mon. Wea. Rev.*, **97**, 163–172.
- Broomhead, D. S., and G. King, 1986: Extracting qualitative dynamics from experimental data. *Physica D*, **20**, 217–236.
- Bryan, K., 1969: A numerical method for the study of the circulation of the world ocean. *J. Comp. Phys.*, **4**, 347–376.
- Collins, M., 2000: The El Niño–Southern Oscillation in the second Hadley Centre coupled model and its response to greenhouse warming. *J. Climate*, **13**, 1293–1312.
- Cox, M. D., 1984: A primitive equation three-dimensional model of the ocean. GFDL Ocean Group Tech. Rep. No. 1, 75 pp.
- Deardorff, J. W., 1972: Parameterization of the planetary boundary layer for use in general circulation models. *Mon. Wea. Rev.*, **100**, 93–106.
- Farrara, J. D., Y.-J. Kim, and C. R. Mechoso, 1997: Simulation of the stratospheric circulation with a general circulation model. *Proc. of Seventh Conf. on Climate Variations*, Long Beach, CA, Amer. Meteor. Soc., 21–26.
- Harshvardhan, R. D., D. A. Randall, and T. G. Corsetti, 1987: A fast radiation parameterization for general circulation models. *J. Geophys. Res.*, **92**, 1009–1016.
- Jin, F.-F., 1997: An equatorial recharge paradigm for ENSO. Part I: Conceptual model. *J. Atmos. Sci.*, **54**, 811–829.
- , and J. D. Neelin, 1993a: Modes of interannual tropical ocean–atmosphere interaction—a unified view. Part I: Numerical results. *J. Atmos. Sci.*, **21**, 3477–3503.
- , and —, 1993b: Modes of interannual tropical ocean–atmosphere interaction—a unified view. Part III: Analytical results in fully coupled cases. *J. Atmos. Sci.*, **21**, 3523–3540.
- , —, and M. Ghil, 1994: El Niño on the devil’s staircase: Annual subharmonic steps to chaos. *Science*, **264**, 70–72.
- Katayama, A., 1972: A simplified scheme for computing radiative transfer in the troposphere. Numerical Simulation of Weather and Climate Tech. Rep. 6, Dept. of Atmospheric Sciences, University of California, Los Angeles, 77 pp.
- Keppenne, C. L., and M. Ghil, 1992: Adaptive spectral analysis and prediction of the Southern Oscillation index. *J. Geophys. Res.*, **97**, 20 449–20 454.
- Kim, Y.-J., and A. Arakawa, 1995: Improvement of orographic gravity-wave parameterization using a mesoscale gravity-wave model. *J. Atmos. Sci.*, **52**, 1875–1902.
- Lacis, A. A., and J. E. Hansen, 1974: A parameterization for the absorption of solar radiation in the earth’s atmosphere. *J. Atmos. Sci.*, **31**, 118–133.
- Latif, M., A. Sterl, E. Maier-Reimer, and M. M. Junge, 1993: Climate variability in a coupled GCM. Part I: The tropical Pacific. *J. Climate*, **6**, 5–21.
- Levitus, S., 1982: *Climatological Atlas of the World Ocean*. NOAA Prof Paper 13, 173 pp.
- , J. Antonov, and T. P. Boyer, 1994: *World Ocean Atlas*. Vol. 5, *Interannual Variability of Upper Ocean Thermal Structure*. NOAA Atlas NESDIS 5, 176 pp. [Available from NODC/NOAA, E/OC5, 1315 East-West Highway, Silver Spring, MD 20910.]
- Li, J.-L. F., C. R. Mechoso, and A. Arakawa, 1999: Improved PBL moist processes with the UCLA GCM. *Proc. of the Ninth AMS Conference on Climate Change*, Dallas, TX, Amer. Meteor. Soc., 423–426.
- Ma, C.-C., C. R. Mechoso, A. W. Robertson, and A. Arakawa, 1996: Peruvian stratus clouds and the tropical Pacific circulation: A coupled ocean–atmosphere GCM study. *J. Climate*, **9**, 1635–1645.
- Manabe, S., and F. Möller, 1961: On the radiative equilibrium and heat balance of the atmosphere. *Mon. Wea. Rev.*, **89**, 503–532.
- McPhaden, M. J., 1999: Genesis and evolution of the 1997–98 El Niño. *Science*, **283**, 950–954.
- Mechoso, C. R., and Coauthors, 1995: The seasonal cycle over the tropical Pacific in general circulation models. *Mon. Wea. Rev.*, **123**, 2825–2838.
- , J.-Y. Yu, and A. Arakawa, 2000: A coupled GCM pilgrimage: From climate catastrophe to ENSO simulations. *General Circulation Model Development: Past, Present, and Future*, D. A. Randall, Ed., Academic Press, 539–575.
- Meehl, G. A., 1990: Seasonal cycle forcing of El Niño–Southern Oscillation in a global coupled atmosphere–ocean GCM. *J. Climate*, **3**, 72–98.
- Mellor, G. L., and T. Yamada, 1982: Development of a turbulence closure model for geophysical fluid problems. *Rev. Geophys. Space Phys.*, **20**, 851–875.
- Nagai, T., T. Tokioka, M. Endoh, and Y. Kitamura, 1992: El Niño–Southern Oscillation simulated in an MRI atmosphere–ocean coupled general circulation model. *J. Climate*, **5**, 1202–1233.
- Neelin, J. D., 1991: The slow sea surface temperature mode and the fast-wave limit: Analytical theory for tropical interannual oscillations and experiments in a hybrid coupled model. *J. Atmos. Sci.*, **48**, 584–606.
- , and F.-F. Jin, 1993: Modes of interannual tropical ocean–atmosphere interaction—a unified view. Part II: Analytical results in the weak-coupling limit. *J. Atmos. Sci.*, **21**, 3504–3522.
- , and Coauthors, 1992: Tropical air–sea interaction in general circulation models. *Climate Dyn.*, **7**, 73–104.
- , D. S. Battisti, A. C. Hirst, F.-F. Jin, Y. Wakata, T. Yamagata, S. Zebiak, 1998: ENSO theory. *J. Geophys. Res.*, **103**, 14 261–14 290.
- Pacanowski, R. C., K. W. Dixon, and A. Rosati, 1991: The GFDL Modular Ocean Model user guide. GFDL Ocean Group, Tech. Rep. 2, 75 pp.
- Philander, S. G. H., 1990: *El Niño, La Niña, and the Southern Oscillation*. Academic Press, 289 pp.
- , R. C. Pacanowski, N.-C. Lau, and M. J. Nath, 1992: Simulation of ENSO with a global atmospheric GCM coupled to a high-resolution tropical Pacific Ocean GCM. *J. Climate*, **5**, 308–329.
- , D. Gu, D. Halpern, G. Lambert, N.-C. Lau, T. Li, R. C. Pa-

- canowski, 1996: Why the ITCZ is mostly north of the equator. *J. Climate*, **9**, 2958–2972.
- Rasmusson, E. M., and T. H. Carpenter, 1982: Variations in tropical sea surface temperature and surface wind fields associated with the Southern Oscillation–El Niño. *Mon. Wea. Rev.*, **110**, 354–384.
- Robertson, A. W., C.-C. Ma, C. R. Mechoso, and M. Ghil, 1995a: Simulations of the tropical Pacific climate with a coupled ocean–atmosphere general circulation model. Part I: The seasonal cycle. *J. Climate*, **5**, 1178–1198.
- , —, M. Ghil, and C. R. Mechoso, 1995b: Simulation of the tropical Pacific climate with a coupled ocean–atmosphere general circulation model. Part II: Interannual variability. *J. Climate*, **8**, 1199–1216.
- Schneider, E. K., B. Huang, and J. Shukla, 1995: Ocean wave dynamics and El Niño. *J. Climate*, **8**, 2415–2439.
- Schopf, P. S., and M. J. Suarez, 1988: Vacillations in a coupled ocean–atmosphere model. *J. Atmos. Sci.*, **45**, 549–566.
- Suarez, M. J., A. Arakawa, and D. A. Randall, 1983: The parameterization of the planetary boundary layer in the UCLA general circulation model: Formulation and results. *Mon. Wea. Rev.*, **111**, 2224–2243.
- Trenberth, K. E., 1998: Development and Forecasts of the 1997–98 El Niño: CLIVAR scientific issues. *Exchanges*, **2**, 4–11.
- Tziperman, E., L. Stone, H. Jarsoh, and M. A. Cane, 1994: El Niño chaos: Overlapping of resonances between the seasonal cycle and Pacific ocean–atmosphere oscillator. *Science*, **264**, 72–74.
- Vautard, R., and M. Ghil, 1989: Singular-spectrum analysis in nonlinear dynamics with applications to paleoclimate time series. *Physica D*, **35**, 395–424.
- Wyrtki, K., 1975: El Niño—the dynamic response of the equatorial Pacific Ocean to atmospheric forcing. *J. Phys. Oceanogr.*, **5**, 572–584.
- Yu, J.-Y., and C. R. Mechoso, 1998: Simulations of Tropical climate and variability with the UCLA coupled atmosphere–ocean GCM. *Proc. of the 1998 Conf. on Mission Earth: Modeling and Simulation of the Earth System*, San Diego, CA, Society for Computer Simulation, 3–8.
- , —, J. D. Farrara, Y.-J. Kim, J.-L. Li, M. Köhler, and A. Arakawa, 1997: Recent development of the UCLA coupled atmosphere–ocean GCM. *Research Activities in Atmospheric and Oceanic Modelling*, A. Staniforth, Eds., WMO Rep. No. 25, 7.81–7.82.
- , and —, 1999a: A discussion on the errors in the surface heat fluxes simulated by a coupled GCM. *J. Climate*, **12**, 416–426.
- , and —, 1999b: Links between annual variations of Peruvian stratocumulus clouds and of SSTs in the eastern equatorial Pacific. *J. Climate*, **12**, 3305–3318.
- Zebiak, S. E., 1989: Ocean heat content variability and El Niño cycles. *J. Phys. Oceanogr.*, **19**, 475–486.
- , and M. A. Cane, 1987: A model El Niño–Southern Oscillation. *Mon. Wea. Rev.*, **115**, 2262–2278.
- Zhang, R.-H., and S. Levitus, 1997: Interannual variability of the coupled tropical Pacific ocean–atmosphere system associated with the El Niño–Southern Oscillation. *J. Climate*, **10**, 1312–1330.